Metal-Organic Frameworks as Platform for the Removal of Per- and Polyfluoroalkyl Substances from Contaminated Waters

Rui Li,[1*], Nayarassery N. Adarsh,[2] Hui Lu[1] and Mario Wriedt[2*]

[1]School of Environmental Science and Engineering, Sun Yat-Sen University, Guangzhou, 510006, China

[2]Department of Chemistry & Biomolecular Science, Clarkson University, Potsdam, New York 13699, USA

Corresponding authors:

RL, Email: lirui253@mail.sysu.edu.cn; Tel: 315-268-3851

MW, Email: mwriedt@clarkson.edu; Tel: 315-268-2355

Lead contact:

MW, Email: mwriedt@clarkson.edu; Tel: 315-268-2355

Keywords: metal-organic frameworks, nanoporous materials, per- and polyfluoroalkyl substances, emerging contaminants, adsorption-based applications, water remediation, water pollution

Summary

Poly- and perfluoroalkyl substances (PFAS) have received considerable attention due to their toxicity, ubiquitous presence, and recalcitrance in the environment. Manufacture and disposal of PFAS-containing products has resulted in PFAS contamination of groundwater and drinking water supplies. Substantial interest and efforts in developing PFAS treatment technologies is triggered since PFAS are associated with numerous adverse health effects. Physical separation using activated carbon and ion exchange is the most widely adopted technique for PFAS removal from contaminated water. However, both adsorbents generally exhibit low PFAS adsorption capacities and/or slow adsorption kinetics. The development of efficient adsorbents is of urgent need. Metal-organic frameworks (MOFs) are an emerging class of hybrid crystalline nanoporous materials, which are composed of inorganic and organic building blocks to form multidimensional networks. Key features—tunable structures and high internal surface areas—render MOFs as ideal platform for PFAS removal from aqueous environments. This review critically examines the application of MOFs for PFAS removal and highlights the structural features of MOFs in context of their PFAS removal performances. Factors affecting the adsorption efficiency, regeneration, and application for PFAS detection are extensively discussed while also providing important insights on design strategies for next-generation MOF materials with improved PFAS removal performances.

1. Introduction

Per- and polyfluoroalkyl substances (PFAS) are a class of anthropogenic chemicals containing a hydrophobic C-F chain and a hydrophilic headgroup. By varying the carbon chain length and the headgroup, over 5000 types of PFAS have been reported to date.[1] PFAS exhibit excellent thermal and chemical stability and surface activity, leading to their wide industrial and commercial applications such as coating for non-stick cookware, aqueous film-forming foams, surfactants in semiconductor fabrication processes, etc. (**Scheme 1**). Due to the disposal of PFAS-containing products and the persistent nature of PFAS molecules, they have been detected in surface water, tap water and drinking water. PFAS are dubbed as "forever chemicals" because they are bioaccumulative in the environment and human body. Recent reports also indicate that they are associated with liver cancer and immune response suppression among other adverse health effects (**Scheme 1**).[2,3] The U.S. Environmental Protection Agency (EPA) issued a health advisory level for the sum of perfluorooctanesulfonate (PFOS) and perfluorooctanoic acid (PFOA) to be below 70 ng/L in drinking water in 2017 while some U.S. states and other countries have more stringent regulations. The increasing concerns over these chemicals have drawn numerous efforts from the government, the industry and academia worldwide to tackle PFAS contamination problems.

Adsorption-based technologies are the most employed methods to treat PFAS-contaminated waters. Among them, activated carbons and ion-exchange (IX) resins are the state-of-art adsorbents. Despite the low cost of granular activated carbon (GAC) and powdered activated carbon (PAC), they are found to be inefficient in removing short-chain PFAS ($4 \leqslant C < 6$ for perfluoroalkyl sulfonates (PFSAs) and $4 \leqslant C < 8$ for perfluoroalkyl carboxylates (PFCAs)).[4,5] Long-chain PFAS ($C \geqslant 6$ for PFSAs and $C \geqslant 8$ for PFCAs), namely PFOS and PFOA, started to phase out of use since the early 2000s and were replaced by short-chain PFAS.[6] Therefore, the removal of short-chain PFAS from contaminated waters is of great importance. In addition, the adsorption capacities of activated carbons are very low which is also coupled with slow kinetics, usually over 24 h. IX resins, as the alternative adsorbent for PFAS removal, can efficiently remove short-chain PFAS. However, they require even longer equilibrium times (over 48 h).[7] Thus, the

development of novel adsorbents featuring large adsorption capacities, fast kinetics, and high selectivity for both long- and short-chain PFAS are of urgent need.

Metal-organic frameworks (MOFs) are a new class of hybrid crystalline nanoporous materials, which are composed of inorganic and organic building blocks to form multidimensional porous frameworks. The general properties and applications of MOFs have been described in numerous review articles before.[8–11] Due to their key features such as tunable structures, large surface areas (up to 7800 m^2/g)[12] and large internal pore volumes (accessible pore volume up to 5.0 cm^3/g)[12], MOFs have been widely used for pollutant removal (e.g., azoles, dyes, selenate) from aqueous environments.[13–15] Large adsorption capacities coupled with fast kinetics for the removal of various pollutants have brought MOFs in the spotlight with numerous reviews extensively discussing their application in water remediation over the past twelve years.[16–21] More recently, MOFs are also identified as advanced material class for the efficient removal of PFAS from water.[22–38] A recent review paper compared the adsorption kinetics, isotherms and mechanisms of MOFs with those of GAC and discussed the factors affecting PFAS removal for both adsorbents.[39] However, this review and related publications focus on the removal of PFOA and PFOS, two long-chain and anionic PFAS whereas the roles of chain length, charge state and functionality of PFAS on removal efficiency are unclear, especially the removal performance of short- and ultrashort-chain PFAS ($C < 4$ for PFSAs and $C < 4$ for PFCAs) and non-ionic PFAS. The role of the MOFs' structural features (e.g., node composition, organic linker type and functionality, pore size and pore volume) on their PFAS adsorption performance has also not been analyzed to date. Another limitation of most reports is that they describe the adsorption performances using lab-prepared samples from deionized water, thus, the performance of MOFs for PFAS removal from water of real contaminated sources remains unknown. Furthermore, the concentrations used in these studies are in mg/L levels whereas in contaminated water (e.g., groundwater) the concentrations of PFAS are in ng/L and/or µg/L levels. Despite the need to investigate the saturation limit which requires high PFAS concentrations (hundreds of mg/L), there is a lack of research using environmentally relevant concentrations. In addition, for practical applications, the reusability of the sorbents is of great importance, but the regeneration of MOFs has not been reviewed to date.

Therefore, as represented in **Scheme 1**, the scope of this review is to systematically analyze the application of MOFs for PFAS (including short- and ultrashort-chain PFAS and non-ionic PFAS) removal with particular focus on: (i) adsorption mechanisms correlated to the node and linker composition and functionality of MOFs and PFAS structure, (ii) the roles of PFAS' molecular structure, MOF particle size and porosity, concentrations of the adsorbent and adsorbate, solution temperature and pH, and water matrix on the PFAS adsorption performance, and (iii) the regeneration of MOFs. Further note that this review discuses PFAS adsorption by MOFs in context with state-of-art adsorbents such as activated carbons and ion exchange resins but the comparison with other emerging adsorbents (covalent organic frameworks, cyclodextrin polymers, etc.) is not within the scope of this review. It should also be noted that this review focuses on the removal of PFAS by MOFs and the comparison between the removal of PFAS and other water pollutants by MOFs is not included given the distinctly different structures of PFAS as compared to other water pollutants (hydrophobic C-F chain and a hydrophilic functional group). Please refer to recent review papers which systematically discuss the application of MOFs for the removal of other emerging water pollutants.[40–42] Following the discussions of PFAS adsorption using MOFs, this review also briefly summarizes the application of MOFs as a pretreatment method for the ultrasensitive detection of PFAS in aqueous media. The review finally concludes with providing guidelines for the design of novel MOF-based adsorbents with potentially improved adsorption capacities and kinetics for the efficient removal of PFAS from contaminated waters.

2. Adsorbent categories, adsorption kinetics, isotherms, and mechanisms

2.1 MOFs and PFAS categories

MOFs were probed as novel adsorbents for PFAS removal from water starting 2015.[34] As of February 2022, Clarivate's Web of Science platform lists a total of 18 research papers[22–38,43] and one review paper[39] which report the adsorption of PFAS using MOFs. Given the more stringent federal regulations and the development of analytical methods with wider PFAS analytes and lower detection limits, this number is expected to increase significantly over the next few years.

Since the first MOFs were discovered in 1999,[44] thousands of MOFs have followed to date, but to be applicable for water remediation they need to fulfill two critical requirements: (i) stability in water under adsorption conditions and (ii) pore apertures and diameters must be at least equal or exceeding the kinetic diameters of given adsorbates. A few percentage of MOFs meet this criteria[11,13–15] and as summarized in **Figure 1**, six MOF families have been investigated for the removal of PFAS from water to date, belonging to the MIL (Materials of Institute Lavoisier),[45] UiO (University of Oslo),[46] NU (Northernwestern University),[47] SCU (Soochow University),[31] ZIF (zeolitic imidazolate framework),[48] and DUT (Dresden University of Technology)[49] families, among other MOFs such as benzenetricarboxylic acid (BTC)-based MOF.[50] These MOFs are composed of a variety of metal nodes and organic linkers while featuring different porosities and topologies. Their structural details are listed in **Table 1**. Key features include pore and aperture sizes ranging from 0.3 to 3.3 nm and pore volumes vary from ~0.1 cm^3/g to ~2.8 cm^3/g. The Brunauer-Emmett-Teller specific surface areas (BET SSA) of investigated MOFs are in the range of 12 to 3100 m^2/g. The composition of metal node and organic linker, and the porosity and particle size of MOFs might impact the adsorption performance and will be discussed in detail in the following sections.

Most of the published work focused on the adsorption of PFOA and PFOS in lab water prepared with deionized water. Li *et al.* recently broadened the PFAS list to eight PFAS classes. As represented in **Figure 2**, these PFAS include (i) PFCAs, (ii) PFSAs, (iii) fluorotelomer sulfonic acids (FTSs), (iv) fluorotelomer carboxylic acids (FTCAs), (v) perfluoroalkane sulfonamide acetic acids (FASAAs), (vi) perfluoroalkane sulfonamides (FASAs), (vii) *N*-methyl perfluoroalkane sulfonamides (MeFASAs), (viii) *N*-[3-(dimethylamino)propyl]-perfluoroalkane sulfonamides (Am-Pr-FASAs), and (ix) perfluorinated alcohols (PFOHs).[25] Among them, the pK_a of PFCAs, PFSAs, FTSs, FTCAs and FASAAs are low (e.g., the pK_a of perfluorobutane sulfonate, PFBS, is -3.3) and they exist in their deprotonated anionic form at environmental relevant pH. FASAs, MeFASAs and PFOHs feature amines and alcohols as functional groups and are non-ionic at near neutral pH. The Am-Pr-FASA family is zwitterionic at near neutral pH. For reference, the detailed molecular structures, pK_a, and $logk_{ow}$ values of all discussed PFAS are listed in

Table 2. The chain length, functionality, and initial concentration of PFAS impact the removal efficiency and mechanisms, which will be discussed in the following sections.

2.2 Adsorption kinetics

A total of twelve studies[22,24,27–35,43] analyzed the adsorption kinetics of PFAS on MOFs. These adsorption kinetics are most commonly described using a pseudo-second-order model which is based on the assumption that surface reactions/interactions occur between PFAS and the adsorbent.[54] Representative pseudo-second-order models for (functionalized) MIL-101, UiO-66, UiO-67 and Fe-based MOFs are shown in **Figures 3A-C**. The adsorption is initially rapid then followed by slow adsorption until equilibrium is reached. The adsorption equilibrium is reached within 2 h for most investigated MOFs which is significantly faster than the state-of-art adsorbents such as GAC (>24 h) and IX resins (50 - 168 h). MOFs UiO-66, SCU-8 and NU-1000 exhibited the fastest kinetics with equilibrium reached within 10 min of contact time due to their suitable porosity and surface chemistry. Among all the reported MOFs, NU-1000 was found to exhibit record fast kinetics with equilibrium reached within one minute for a range of PFSAs and PFCAs.[26] This can be attributed to the NU-1000's large pore apertures and pore sizes (hexagonal mesopore and trigonal micropore with diameters of 33 and 13 Å, respectively) which facilitate the diffusion of PFAS molecules into the pores. Its high surface area (2210 m^2/g) and large pore volume (1.56 cm^3/g) are additional factors that contribute to the ultrafast kinetics of NU-1000. Some MOFs, however, exhibit relatively slow kinetics. For example, Cr/Fe-MIL-101 requires over 100 h to reach equilibrium and the adsorption profiles of PFOS were fitted to a double exponential decay function.[33] MIL-96-hydrolyzed polycrylamide (RHPAM2, added to control the particle size, crystal morphology and to modify the functionality) also suffers from slow kinetics as the addition of hydrolyzed polyacrylamide significantly blocks the pore access.[22] The Elovich kinetics model provide a better fit compared to the pseudo-second-order kinetics model for PFOA adsorption on MIL-96-RHPAM2, indicating the adsorption proceed in a highly heterogenous system. The intraparticle diffusion model is another model used to describe the adsorption kinetics. This model assumes boundary layer diffusion and external diffusion are negligible in

controlling the adsorption rate and intraparticle diffusion is the only rate-limiting process, not surface adsorption. Multilinearity in the plot calculated by the intraparticle diffusion model was observed for UiO-66,[35] Fe-BTC, MIL-100-Fe, and MIL-101-Fe,[29] indicating there are different stages to the adsorption process. It should be noted that the adsorption profiles of PFAS might be fitted into multiple kinetic models at the same time. For example, the kinetic data of defective UiO-66 materials [35] and Fe-based BTC- and MIL-MOFs[29] can be well fitted into both the pseudo-second order model and the intraparticle diffusion mode. We can speculate from the above kinetic models that the porosity and particle size of MOFs play a key role in adsorption kinetics which will be discussed in detail in Section 3.1.

2.3 Adsorption isotherms

Classic Langmuir and Freundlich isotherm models are widely used in a total of thirteen studies [24,26–32,34–37,43] to assess the adsorption isotherms of PFAS on MOFs. The Langmuir isotherm model exhibits a better fit for PFOA and PFOS for most MOFs studied, suggesting that PFAS adsorbs on MOFs in a monolayer fashion at a single adsorption site. Representative Langmuir and Freundlich fits for MIL-101 derivatives, UiO family and Fe-based MOFs are represented in **Figures 3D-F**. However, Sini *et al*.[24] observed a better fit of the Freundlich isotherm model for the adsorption of PFOS and PFOA on UiO-67, indicating a multi-layer process which is limited by the diffusion inside the cavity as a result of the increasing cavity sizes. Different isotherms are observed for short-chain (C4) PFBS. Clark *et al*.[35] found the Freundlich isotherm model applies to PFBS adsorption on defective UiO-66-25 while Li *et al*.[26] reported good fit for both the Langmuir (slightly better fit) and Freundlich isotherms for PFBS on NU-1000. Multilayer adsorption of PFBS likely plays a more significant role for UiO-66-25 due to the excess porous nature of the defective material and the short carbon chain of PFBS. The adsorption of PFBS on NU-1000 using both isotherm models suggest a monolayer adsorption at a single site as well as heterogenous adsorption with different adsorption energies at multiple adsorption sites. This finding is in accordance with the heteroporosity of NU-1000. In summary, the best fit model depends on specific conditions. Adsorption isotherms can be

greatly influenced by the structural features of PFAS and MOFs, water matrix and concentrations of adsorbent and adsorbate (will be discussed in detail in Section 3).

2.4 Adsorption mechanisms

Upon exposure to MOFs, PFAS molecules diffuse into their pores and bind non-covalently with the metal node and/or the organic linkers. Evidence for the successful loading of PFAS molecules onto MOFs lies on the decrease of their BET SSA and pore volume (e.g., the BET SSA of NU-1000 decreased from 2300 to 1600 m^2/g and the pore volume decreased from 1.56 to 0.98 cm^3/g upon saturation with PFBS) and the appearance of new bands on the Fourier-transform infrared spectroscopy (FT-IR) spectrum representing C–F stretching at 1000-1400 cm^{-1}, C=O stretching at 1730 cm^{-1} (e.g., PFOA) and S=O stretching at 1000 cm^{-1} (e.g., PFBS and PFOS).[26,29,30,32,33] Representative N_2 isotherms, pore volume distribution, and vibrational spectroscopy data are shown in **Figures 4A-C**. X-ray photoelectron spectroscopy (XPS) is another important tool to verify PFAS adsorption into MOFs. As representative examples, the XPS spectra for PFBS@NU-1000 and PFOA@MIL-101-Fe show the formation of distinct F 1s and S 2p binding energies upon PFAS@MOF binding while their respective metal node binding energies (Zr 3d and Fe 2p) remain unchanged or slightly shifted as compared to the pristine MOFs.[26,28,29] The morphology and structural integrity of MOFs remain largely unchanged after PFAS adsorption, which is evident from unchanged scanning electron microscopy (SEM) images (Figure 4D) and the powder X-ray diffraction (PXRD, **Figure 4E**) patterns before *vs.* after adsorption.[26,33]

The detailed PFAS@MOF adsorption mechanisms depend on the general structural features of PFAS (C–F chain length, functionality and charge state) and MOFs (node composition, organic linker type and functionality of the organic linker) and can be categorized into five PFAS@MOF interaction types: (i) electrostatic; (ii) Lewis acid-base; (iii) hydrophobic; (iv) hydrogen bonding; and (v) van der Waals interactions.

Electrostatic interactions between deprotonated PFAS molecules and cationic metal nodes or protonated organic ligands play a predominant role in the adsorption of anionic PFAS (**Figure 5A-C**). As

listed in **Table 2**, most PFAS have a low pK_a and therefore exist in their anionic form in aqueous solutions such as PFOA (pK_a = -0.5), PFOS (pK_a = -3.3) and 6:2 FTS (pK_a = 0.36). MOFs contain positively charged metal centers (e.g., Al^{3+} for MIL-96[22] and Th^{4+} for SCU-8[31]) and thus bind strongly with negatively charged PFAS. The organic linker in some MOFs can be also protonated which can readily bind with anionic PFAS electrostatically. For example, Liu *et al.* report that carboxyl groups of the terephthalic acid linker in MIL-101(Cr) are protonated at pH < 5, which provide strong binding sites for PFOA.[34] Similarly, Clark *et al.* show that defective UiO-66-10 exhibits a larger adsorption capacity as compared to UiO-66-25 which originates from UiO-66-10 having a lower Cl^- content at its Zr_6-nodes and linker defect sites and thus less electrostatic repulsion from PFOS.[35] MOFs containing an organic moiety with a higher pK_a is found by Chen *et al.* to have a stronger affinity to deprotonated PFOA or PFOS due to their higher surface charge.[30] For example, the adsorption capacity of ZIF-8 which contains 2-methylimidazole (pK_a = 7.9) as ligand is significantly higher than that of ZIF-7 which bears benzimidazole as ligand (pK_a = 5.3).[30] In addition, significant PFAS adsorption capacities are frequently observed for amino-functionalized MOFs. Their amino groups are generally protonated ($-NH_3^+$) in aqueous solution and thus resulting in enhanced interactions with the deprotonated sulfonic ($-SO_3^-$) or carboxyl ($-COO^-$) groups of PFAS.[22,34,36] For example, a superior PFOA adsorption capacity was observed for MIL-96-RHPAM2 as compared to the less performing classic MIL-96. Azmi *et al.* attributed this to the formation of electrostatic interactions between the anionic carboxylate of PFOA and the amine functionality present in the HPAM backbone as evident from distinct IR bands representing anionic PFOA on the FTIR spectrum after adsorption.[22] Though the introduction of functionality into MOFs can advance their surface chemistry, one should be advised that the approach of functionalization should be carefully chosen to avoid the introduction of any potential steric hindrance (e.g., bulky aromatic amines) and thus impacting the MOF's pore apertures. Further electrostatic PFAS@MOF binding can be characterized based on an anion exchange mechanism. For example, the metal nodes of NU-1000 (**Figure 5A**) and MIL-101 feature terminally coordinated hydroxo anions which were found to be exchangeable with the respective deprotonated carboxylic/sulfonic acid head groups of PFAS.[26,34] Evidence for the replacement of such hydroxo anions is demonstrated from spectroscopic data

including the reduction of intensity or vanishment of distinct bands representing O−H stretching and bending (e.g., 3350 and 1410 cm^{-1} for FTIR, and 3650 cm^{-1} for diffuse reflectance Frontier-transform infrared spectroscopy, DRIFTS as shown in **Figures 4C** and **4F**).[26,29] Electrostatic interactions might play a minor role for non-ionic PFAS (e.g., FASAs) due to lacking charges within these molecules. However, *Li et al.* report an alternative mechanism for FASA binding. For example, the amine group in C8 perfluorooctanesulfonamide (FOSA) can deprotonate the μ_3-bridging hydroxo groups of NU-1000's Zr_6-nodes which can lead to strong electrostatic μ_3-O^{2-}−NH_3^+ interactions.[25]

Lewis acid-base interactions between the functional groups of PFAS and the metal nodes of MOFs are the key mechanism for non-ionic PFAS adsorption and also play a role in anionic PFAS adsorption (**Figures 5B and 5D**). The amine groups of non-ionic FASAs are characterized as hard base and can interact strongly with hard acids such as the Zr nodes in UiO and NU family MOFs.[25] For anionic PFCAs and PFSAs, their carboxylate or sulfate groups are also considered as hard base and can interact strongly with the hard acid Zr and Cr nodes of NU and MIL family MOFs, respectively. For example, *Liu et* al. report the formation of a stable complex from the interactions of PFOA (the Lewis base) and unsaturated Cr sites of MIL-101 (the Lewis acid).[34] Generally, the higher the acidity of the metal node, the stronger the acid-base interaction of PFAS@MOF binding. This hypothesis is corroborated from the adsorption of PFOS by Cr- and Fe-MIL-101. While both MOFs are composed of identical organic ligands and share similar porosity characteristics, Cr-MIL-101 exhibits a larger PFOS adsorption capacity as compared to Fe-MIL-101 since Cr is the harder Lewis acid compared to Fe as confirmed by respective metal node binding energy calculations using XPS.[33] Moreover, a higher number of active metal sites at the MOF nodes leads to a better adsorption performance. For example, Fe-BTC exhibits higher PFOA adsorption capacity compared to MIL-100-Fe due to the extra Lewis acid sites on Fe-BTC although both MOFs are composed of the same organic ligand.[29] Zhao *et al.* also partially attributed the best PFOS adsorption performance of MIL-53-Al to its defect-introdcued highest unsaturated metal active sites.[28] This study also points out that the general PFAS adsorption performance of MOFs with different metal nodes might change if there is a significant change in the corresponding surface areas and pore sizes,[28] which will be discussed in detail in the following

sections below. On the other hand, Lewis acid-base complexation between unsaturated Zr-sites within defective UiO-66 and the sulfonate headgroups of PFOS was ruled out as the dominating mechanism since the FTIR spectra of the pristine MOF *vs.* after PFOS adsorption did not show any significant changes to the band region corresponding to the Zr cluster.[32,35]

Non-covalent hydrophobic interactions between the C-F chains of PFAS and the MOFs' hydrophobic pockets originated from specific arrangements of the ligands' aromatic rings constitute another important mechanism for PFAS@MOF adsorption. PFAS molecules contain hydrophobic poly- or perfluorinated alkyl tails regardless of their functionality and charge state which are especially dominant for long-chain PFAS. The organic linkers of MOFs which are typically composed of functionalized and/or fused benzene rings can non-covalently bind with these C-F chains of PFAS *via* hydrophobic interactions. For example, the PFOA adsorption capacity of 169 mg/g for Basolite A100 is facilitated from the stacked C-F chains of PFOA along the channel pores of Basolite A100 which are decorated by benzene rings of the terephthalic acid (BDC) ligand (**Figure 5B**).[27] In contrast, MOF-801 contains hydrophilic fumaric acid as its organic linker, leading to the low PFOS adsorption capacity of 48 mg/g.[36] Defective UiO-66-25 is missing more organic linkers and is therefore more hydrophilic compared to UiO-66-10, which partially accounts for its lower PFOS adsorption capacity (350 *vs.* 375 mg/g).[35] The increase in C-F chain length of PFAS leads to an increase in hydrophobicity thus a stronger hydrophobic interaction and higher adsorption capacity. For example, the adsorption capacity of PFOS (C8) on NU-1000 is 622 mg/g whereas that for PFBS (C4) is 404 mg/g.[26] The hydrophobicity of short- (e.g., PFBS) and ultrashort-chain (e.g., trifluoroacetic acid (TFA, C2) PFAS is weak thus the dominant mechanism for their adsorption is mostly of electrostatic nature since hydrophobic interactions are weak or absent. For non-ionic PFAS, hydrophobic interactions play an important role in addition to acid-base interactions due to the lack of electrostatic interactions. Perfuorooctanol (C8, non-ionic) adsorption on UiO-66 and UiO-66-F is reported by Sini *et al.* to be driven by hydrophobic interactions between their hydrophobic moieties due to lacking negative charges of the non-ionic PFAS.[32]

Hydrogen bonding is another driving force for PFAS adsorption which can be formed between the functional groups of PFAS (e.g., sulfonate or carboxylate groups) and coordinating water molecules of the MOFs' metal nodes (**Figure 5B**) or perfluorinated functional groups of the MOF ligands. For example, Li *et al.* reports that the sulfonate group of PFOS forms firm hydrogen bonding with coordinating water molecules inside the channel pores of SCU-8, which plays an important role the adsorption process.[31] Furthermore, perfluorinated MOFs (e.g., UiO-66-F4 and F-MOF) are found to exhibit significant PFAS adsorption capacities owed to strong hydrogen bonding and attractive F-F interactions between the MOFs' fluorinated backbones and the C-F chains of PFAS.[32,38]

Van der Waals interactions between the carbon chain of PFAS and the organic linker of MOFs can also contribute to the adsorption process. For example, Azmi *et al.* reports that the main skeleton of HPAM $(CH_2\text{-}CH)_n$ on MIL-96-RHPAM2 can form van der Waals interactions with the C-F chain of PFOA (8 carbons on the linear chain).[22] In a further example, Li *et al.* show that the calculated van der Waals *vs.* the electrostatic interaction energies between PFOS and SCU-8 decrease significantly over time indicating strong van der Waals and electrostatic interactions collectively drive the early adsorption process in addition to hydrophobic interactions.[31]

It is important to note that the adsorption process can proceed in different stages with each stage driven by different mechanisms or by the synergistic effect of multiple mechanisms.[29,31] Evidence for this multi-stage mechanism lies in the multiple linearity relationship of the intraparticle diffusion mode as discussed in Section 2.2. Li *et al*. calculated the free energy of PFOS@SCU-8 binding and divided the process into five stages: i) sulfonate group of PFOS is attached to SCU-8 *via* electrostatic interactions with the hydrophobic tail exposed to water; ii) the hydrophobic tail of PFOS enters the SCU-8 channels; iii) sulfonate group of PFOS forms hydrogen bonding with coordinated water molecules on the node with a significant portion of the PFOS tail stacked on the inner wall of SCU-8; iv) hydrophobic tail of PFOS is fully pushed into the channels of SCU-8 *via* hydrophobic interactions; v) tail of PFOS is fully stacked within the hydrophobic channels of SCU-8.[31] However, similar multi-stage adsorption processes are largely unexplored for other MOF types.

3. Factors affecting PFAS adsorption

As represented in **Scheme 2**, PFAS removal efficiencies can be greatly influenced by the structure, porosity, and particle size of MOFs, PFAS structure (chain length, functionality, and charge state), concentrations of adsorbent and adsorbate, solution temperature and pH, and water matrix

3.1 The role of MOF structure

An understanding of structure-activity relationships governing the PFAS@MOF adsorption processes is instrumental for the successful design of MOF candidates for PFAS remediation from contaminated waters. Single-crystal X-ray diffraction enables precise structural characterization of MOFs due to their high crystalline nature and frequent availability of single crystals. As a result, their crystal structures can be elucidated with an atomic resolution which offers vital insights for developing a strategy for PFAS adsorption. The metal node composition, functionality present in ligand, pore size/shape of the framework and coordinatively unsaturated metal centers are fundamentally important structural parameters which determine the affinity of MOFs to adsorb PFAS. Based on the crystal structures of the MOFs discussed in this review (**Figure 1** and **Table 1**), we can conclude that MOFs capable of occluding PFAS molecules in their crystal lattice through the combination of various ionic, electrostatic, and hydrophobic interactions, have a strong tendency to form PFAS@MOF composites. In addition, such MOFs must exhibit appropriate pore apertures and pore shapes matching or exceeding the kinetic diameters of PFAS. For reference, we summarize important structural characteristic of respective of MOFs covered in this review below.

The four ZIFs possess an identical node composition of [Zn-N_4] consisting of Zn(II) cations tetrahedrally coordinated by N atoms of four 2-methyl imidazole ligands.[30,37] In the crystal structures of ZIF-7, ZIF-8 and ZIF-67, the metal-ligand coordination results in 3D porous structures possessing sodalite topology (*sod*) with pore sizes of 0.3, 1.16 and 1.18 nm, respectively.[37] ZIF-L exhibits a 2D layered structure which further extends into a porous network with *sod* topology and pore size of 0.34 nm. Notably, the ligand 2-methyl imidazole in ZIF-L exists in both protonated and deprotonated forms. In summary, despite

of lacking functionality provided from either the ligand or metal node, all these ZIFs showed reasonable PFAS adsorption due to their pore sizes ranging with the kinetic diameters of adsorbed PFAS.

The Zr(IV)-based MOFs UiO-66, UiO-67 and MOF-801 possess the same metal node composition of $[Zr_6(\mu_3\text{-}O)_4(\mu_3\text{-}OH)_4(-CO_2)_{12}]$.[24,25,32,36] In their crystal structures, the isostructural MOFs UiO-66 and UiO-67 feature tetrahedral [0.8 nm for UiO-66 and 1.2 nm for UiO-67] and octahedral [1.1 nm for UiO-66 and 1.6 nm for UiO-67] cages with possessing an overall face-centered cubic (*fcu*) topology. The hydroxyl functionality present in their nodes represent potential hydrogen bonding sites for PFAS while their aromatic ligands (BDC in UiO-66 and BPDC in UiO-67) contribute to hydrophobic PFAS@MOF interactions. Interestingly, defective UiO-66 shows twice the PFOS adsorption capacity compared to its non-defective counterpart. The pore defects not only result in a general increase of surface area but also induce coordinatively unsaturated Zr sites which are instrumental for ionic binding of the PFOS' sulfonic head groups. Larger cavity size and stronger hydrophobic interactions (due to two aromatic rings of the BPDC ligand) are the factors for superior PFOA and PFOS adsorption capacity of UiO-67 as compared to UiO-66 (only one aromatic ring in the BDC ligand). The fluorinated counterpart of UiO-66 shows enhanced PFOA and PFOS adsorption capacities as compared to pristine UiO-66 due to increased hydrophobic interactions involving the fluorinated cavity of the framework and PFAS. Among various reported UiO-66 derivatives, UiO-66-NH_2 exhibits the best PFOS adsorption capacity despite its significantly smaller surface area as compared to pristine UiO-66. The amino group enables strong electrostatic interactions with the sulfonic groups which is a crucial factor for the superior PFOS adsorption. In contrast to the UiO family MOFs, the structure of MOF-801 contains three distinct pores (two tetrahedral and one octahedral cage sizing 0.56, 0.48, and 0.74 nm, respectively).[36] However, the PFOS adsorption capacity of MOF-801 is significantly less than that of UiO MOFs. One can speculate that the presence of the hydrophilic fumaric acid ligands results in preferred water adsorption over PFOS *via* hydrophilic interactions.

The Zr(IV)-based MOF NU-1000 is composed of $[Zr_6(\mu_3\text{-}O)_4(\mu_3\text{-}OH)_4(H_2O)_4(OH)_4(\text{-}CO_2)_8]$ nodes and the tetratopic ligand 1,3,6,8-tetrakis(p-benzoate)pyrene. Its network structure is of *csq* topology[25,26] and possesses a binary pore system featuring mesoporous hexagonal channels and

microporous triangular channels sizing 3.3 and 1.3 nm, respectively, in their diameters. Interestingly, both pores are interconnected by 0.8 × 1.0 nm windows which enables an enhanced interchannel diffusion of PFAS. NU-1000 shows an exceptional high PFAS adsorption *via* a combination of ionic and hydrophobic interactions. The terminally coordinating hydroxo groups of the Zr_6 node can undergo ion exchange with the anionic head groups of PFAS while their perfluorinated alkyl tails are stabilized by hydrophobic pockets formed from the pyrene ligands.

SCU-8 is a Th(IV)-based MOF composed of $[Th_3(\mu_3\text{-}O)(H_2O)_{3.78}(\text{-}CO_2)_9]$ nodes and tri-carboxylic acid ligands forming a 3D cationic network structure of *flu* topology featuring 1D hexagonal tubular channel pores sizing 2.2 × 2.2 nm.[31] The cationic nature of this MOF enhances the adsorption of anionic PFAS through ionic interactions.

The isostructural MOFs MIL-53(Fe) and MIL-53(Al) are composed of BDC linkers and $[Fe(\mu_2\text{-}OH)_2(\text{-}CO_2)_4]$ and $[Al(\mu_2\text{-}OH)_2(\text{-}CO_2)_4]$ nodes, respectively.[28] The interconnection of these two building blocks results in a porous structure of *sra* topology featuring 1D channels sizing around 0.9 nm, respectively. Interestingly, MIL-53(Al) possesses a slightly higher surface area as compared to MIL-53(Fe) which is also reflected in more efficient PFOS adsorption.

MIL-96(Al) is a BTC-based MOF possessing three metal nodes of composition $[Al_3(\mu_3\text{-}O)(H_2O)_3(\text{-}CO_2)_6]$, $[Al(\mu_2\text{-}OH)_2(\text{-}CO_2)_4]$ and $[Al(\mu_2\text{-}OH)_3(H_2O)(\text{-}CO_2)_2]$.[22] Its honeycomb-like structure exhibits a ternary pore system with respective cages sizing 0.8, 0.25-0.35 and 0.27 nm. Significant PFOA adsorption is observed when modified with polyacrylamide (MIL-96-RHPAM2) enabled by strong NH_2—PFOA electrostatic interactions.

MIL-100(M) and MIL-101(M) with M = Fe(III) and Cr(III)) are composed of ligands BTC and BDC, respectively, while possessing identical octahedral metal(III) oxide nodes of composition $[M_3(\mu_3\text{-}O)(\text{-}CO_2)_6(OH)]$. The 3D porous structure formed from these building blocks is of *mtn* topology. The only structural difference in terms of porosity between these two MOFs is the pore size of their mesoporous cages: 2.4 and 2.9 nm for MIL-100, and 2.7 and 3.4 nm for MIL-101. Moreover, the aperture size of their pentagonal and hexagonal windows also show variance: 0.5 and 0.86 nm for MIL-100, and 1.17 and 1.6

nm for MIL-101.[29] While MIL-100 shows promising PFOS adsorption due to strong metal—sulfonic acid interactions, MIL-101(Cr) and its amino functionalized derivatives feature significant PFOA adsorption due to the synergistic combination of anion-exchange, Lewis acid/base complexation between PFOA and Cr(III), and electrostatic interaction between PFOA and the protonated carboxyl groups of BDC.

DUT-5 is a MIL-56 analogue composed of $[Al(\mu_2\text{-}OH)_2(\text{-}CO_2)_4]$ nodes and the ligand BPDC. The A(III) ions are octahedrally coordinated by six oxygen atoms originating from four carboxylate and two hydroxyl groups. The extended coordination of Al–OH-chains with BPDC ligands leads to the formation of a 3D porous framework with rectangular channels sizing 1.1 × 1.1 nm.[43]

The crystal structure of MIL-125-Ti-NH_2 is formed from cyclic octamers of edge- and corner-sharing $[Ti(\text{-}CO_2)_4(OH)_2]$ octahedra and BDC as the ligand.[23] The resulting framework possesses tetrahedral and octahedral cages sizing 0.613 and 1.255 nm, respectively, with respective pore apertures sizing around 0.5-0.7 nm. The amino group present in the framework allows to form strong hydrogen bonding interactions with PFAS.

3.2 The role of MOF surface area, particle size and porosity

The specific surface area of MOFs generally plays a role in the adsorption of PFAS, however, its role is not dominant. Zhao *et al*. and Endoh *et al*. attributed the significant PFAS adsorption capacities of MIL-53-Al and UiO-66 partially to their high surface areas.[28,36] It is undeniable that the large surface areas of MOFs (up to 7800 m^2/g) facilitates the contact between MOFs and PFAS, especially when comparing with other adsorbent such as GAC and IX resins whose surface areas are significantly lower than MOFs (usually hundreds of m^2/g).[22] On the other hand, other reports show that the surface area is not the dominant factor controlling the adsorption process.[22,29,34,36] For example, MIL-96-RHPAM2 exhibits a relatively small surface area (75 m^2/g) while its PFOA adsorption capacity (340 mg/g) is comparable with other MOFs with surface area larger than 1000 m^2/g.[22] The reason for the surface area independent adsorption performance lies in the surface chemistry, which also plays a key role in the adsorption process. For example, despite the decrease of surface area induced by the functionalization, MIL-101-Cr-quaternized *N*,*N*-

dimethylethylenediamine (QDMEN) exhibits significantly higher PFOA adsorption capacity than the pristine MIL-101-Cr (754 *vs.* 460 mg/g) due to additional electrostatic interactions between the amine moieties and PFOA.[34] A similar example is the higher PFOS adsorption capacity of UiO-66-NH_2 compared to pristine UiO-66 (512 *vs.* 346 mg/g).[36] Another example showing the surface chemistry outperforming the SSA effect is the superior PFOA adsorption capacity of Fe-BTC over that of MIL-101-Fe and MIL-100-Fe despite the lowest surface area of Fe-BTC (1051 m^2/g), attributing to the presence of extra Lewis acid sited on the Fe-BTC thus enhancing the acid-base interaction.[29]

The particle size of MOF materials determines the diffusion rate and access of PFAS molecules to adsorption sites thus playing an important role in the adsorption kinetics. Increasing the particle size increases the diffusion length inside MOFs thus prolonging the equilibrium time.[22] Konno *et al.* observed that equilibrium was reached more rapidly (5 *vs.* 24 h) using nanoZIF-67 (150 nm) compared to macroZIF-67 (2.95 μm) which was attributed to the smaller intraparticle diffusion length of the smaller crystals thus providing more micropore entrances per unit weight.[37] The adsorption capacity, however, is notably not impacted by the crystal size due to the similar BET surface area and micropore volume of nanoZIF-67 and macroZIF-67, respectively. They concluded that downsizing is only effective in improving the adsorption rate. In addition, compared to nonporous materials such as IX resins, Liu *et al.* report that the uniform pores of the MIL family (e.g., MIL-101-Cr-QDMEN) greatly promote the internal diffusion of PFAS resulting in the orders of magnitude faster adsorption rates (2.1×10^{-4} *vs.* 8.1×10^{-7} g mg^{-1} min^{-1}).[34]

Further important factors for efficient PFAS adsorption are the MOF's pore size and aperture and their accessible pore volume. The MOF's pore size needs to be in the range of or larger than the kinetic diameters of PFAS molecules. For example, the diameter of PFOS is 0.65 nm calculated based on the respective van de Waals radii.[36] The pore diameter of UiO-66-NH_2 ranges between 0.37 and 0.92 nm so Endoh *et al.* concluded that PFOS can easily diffuse into the micropores.[36] Furthermore, the larger the pore size and pore volume the larger the adsorption capacity seems to be a plausible statement but it should be noted that the role of pore size and volume can be overridden by the surface chemistry as described above. For example, MIL-53-Al with biphenyl-4,4'-dicarboxylic acid (BPDC) as the linker exhibits a higher

adsorption capacity (305 mg/g) compared to MIL-53-Al with BDC (66 mg/g) due to the longer ligand which contributes to the larger 1D channel window and provides more PFOS entry.[28] Another example of the positive effect of channel window size on PFOS adsorption capacity is the comparison of UiO-67 with BPDC (583 mg/g) and UiO-66 with BDC (160 mg/g).[24] The systematic introduction of missing ligand defects into MOFs is a further strategy to increase pore sizes while increasing the number of unsaturated metal centers to bind with PFAS at the same time. This has been first demonstrated by Clark *et al.* who report that the maximum PFAS adsorption capacity is observed for defective UiO-66 due to the presence of large pore defects (130 mg/g of PFOS for pristine UiO-66 *vs.* 620 mg/g for defective UiO-66-10).[35] On the contrary, UiO-66-NH_2 exhibited a higher PFOS adsorption capacity compared to pristine UiO-66 (512 *vs.* 346 mg/g) despite its smaller pore volume (256 *vs.* 367 cm^3/g), attributing to the additional electrostatic interactions between the added amine moieties and PFOS.[36] Another example is ZIF-7 which exhibits a higher PFOA adsorption capacity (22 mg/g) than activated carbons and zeolites despite its lower pore volume and surface area. Dominating factors for this observation are the presence of benzimidazole within its framework with generally possess a strong affinity to PFOA.[30]

3.3 The role of PFAS structure

The chain length, functionality, and charge state of PFAS molecules can greatly impact the adsorption mechanism and efficiency but the roles of these parameters are largely underexplored since most work in the PFAS@MOF field focuses on the removal of anionic and long-chain PFAS, namely PFOA and PFOS. Longer chain PFAS show higher adsorption capacity, which is widely reported for a variety of adsorbents including GAC, IX resins and covalent organic frameworks (COFs).[55,56] PFAS with longer chain exhibit higher hydrophobicity thus enhancing hydrophobic interactions between the C-F chain of PFAS and the hydrophobic pockets of MOFs. For example, the adsorption capacities of short-chain PFBS and perfluorobutanoic acid (PFBA) are lower than that of PFOS and PFOA on both NU-1000 and defective UiO-66 (162-404 mg/g *vs.* 350-622 mg/g).[26,35] Ultrashort-chain PFAS can also be also rapidly removed by MOFs despite their relatively lower adsorption capacity compared to longer-chain PFAS due to the lack of

hydrophobic interactions. For example, the adsorption capacity of trifluoroacetic acid (TFA, C2) is 201 mg/g on NU-1000.[26] This efficiency significantly outperforms state-of-art GAC which is unable to remove short and ultrashort-chain PFAS.

The functional group of PFAS plays an important role in the PFAS removal process since it determines the hydrophilicity and charge state of PFAS molecules. It should be noted that the role of functional group on the overall removal efficiency should be discussed for PFAS with the same C-F chain length (e.g., PFOA *vs.* perfluoroheptane sulfonate (PFHpS)) instead of the same carbon number (e.g., PFOA *vs.* PFOS). In a recent study, Li *et al.* systematically investigated the removal of eight PFAS families from contaminated groundwater using NU-1000.[25] They observed a higher adsorption capacity of PFSAs over that of PFCAs because the sulfonate group is considered a harder base compared to the carboxylate group thus exhibiting stronger acid-base interaction with the hard acid Zr_6 node. Higher removal of FTCAs was found compared to PFCAs attributing to the extra -CH_2 units thus bearing higher hydrophobicity and concurrently stronger hydrophobic interactions. Similarly, the removal capacity of MeFASAs and Am-Pr-FASAs are higher compared to FASAs due to their larger molecular size.[25]

Non-ionic FASAs are observed to exhibit higher removal compared to anionic PFSAs with the same C-F chain length. Li *et al.* report the removal efficiency of C6 perfluorohexane sulfonate (PFHxS) in NU-1000 is 68% whereas that for C6 perfluorohexanesulfonamide (FHxSA) is 91%.[25] This preferential adsorption might be originated from FASAs' amine group (strong base) which interacts strongly with the Zr_6 node on NU-1000 *via* acid-base interactions. In addition, the amine groups of FASAs can deprotonate the μ_3-bridging hydroxo groups of the Zr_6 nodes which can lead to strong electrostatic μ_3-O^{2-}—NH_3^+ interactions, resulting in the higher removal of FASAs compared to FASAAs.[25]

3.4 The role of the concentrations of adsorbent and adsorbate

The dosage of MOF adsorbent is another factor impacting the PFAS adsorption rate. Listed in **Table 1**, the typical concentration of MOFs ranges 0.1 - 10 g/L and it is observed that the increase of adsorbent dosage generally increases the PFAS removal efficiency. For example, Konno *et al*. tested the adsorption of PFOS

using 0.5 and 5 mg/L ZIF-67 and concluded that increasing the dosage improves the adsorption rate due to the increase in available sites at the adsorbent surface.[37] Yang *et al*. also observed some minor positive correlation between the dosage of Fe-BTC and the removal rate of PFOA using the response surface methodology.[29]

Most studies tested PFAS adsorption with initial concentrations in mg/L or g/L level (as high as 5 g/L). However, PFOS and PFOA have been largely phased out of use since 2006 thus their concentrations (e.g., in industrial effluents) are orders of magnitude lower now. The choice of such high PFAS concentrations is to evaluate the saturation limits and to assess the longevity and lifetime of adsorbents in practical use. However, great care must be taken in performing any adsorption testing using such high PFAS concentrations since the adsorption process (especially that of long-chain PFAS) might be impacted by the formation of micelles. For example, the critical micelle concentration (CMC) of PFOS is 4 g/L (8 mM) and concentrations above this value will lead to the formation of PFOS micelles. PFOS micelles are composed of hydrophobic cores consisting of perfluorinated alkyl chains and hydrophilic shells containing sulfonate groups. As a result, the formation of PFOS micelles would force the sulfonate groups to interact with the adsorption sites on the MOFs thus enhancing the adsorption performance.[33] It should also be noted that the formation of micelles changes the size of PFAS molecules which might affect the diffusion of micelles into the MOF pores. Furthermore, the role of initial concentration of PFAS (below CMC) on their removal using MOFs seems to be insignificant as observed for numerous MOFs.[26,29,36] For example, the adsorption of PFBS at 10 - 100 mg/L was investigated using NU-1000 and the equilibrium was reached within one minute regardless of the initial concentration of PFBS.[26] In another example Yang *et al*. showed that the increase of PFOA concentration leads to an insignificant increase of the removal rate.[29]

In groundwater and drinking water, PFAS usually ranges at the ng/L to μg/L level. For reference, the EPA's health advisory for the sum of PFOA and PFOS concentration in drinking water is 70 ng/L. Concentrations within those levels should be selected to test the performance of MOFs under realistic environmental relevant conditions. Li *et al*. found that SCU-8 can rapidly reduce the PFOS concentration from 1 μg/L to 21 ng/L.[31] A recent study from 2021 examined contaminated groundwater for the adsorption

of 28 PFAS with concentrations ranging from 3 ng/L to 260 μg/L using NU-1000, UiO-66 and ZIF-8.[25] The adsorption equilibria were reached shortly after the exposure regardless of the initial concentrations of the PFAS. The statistical analysis from this work further revealed that the initial concentrations of PFAS has a negligible effect on their adsorption performance. In addition to the adsorption of PFAS in ng/L, g/L and mg/L levels, MOFs have also been used as adsorbents coupled with chromatography for the ultrasensitive detection of PFAS (low ng/L level), which will be discussed in section 5.

3.5 The role of solution temperature

The effect of solution temperature on PFOA and PFOS adsorption was studies in the range of 293 - 318 K. The increase of temperature leads to the increase in adsorption rate and capacity mostly due to the enhanced diffusion of PFOA and PFOS into the cavity of MOFs.[24,27,32] The thermodynamic parameters of the adsorption process can be calculated using the Van't Hoff equation. The positive value of ΔH^0 and the negative value of ΔG^0 indicate the adsorption process is endothermic and spontaneous whereas the positive value of ΔS^0 suggests the adsorption leads to an increase in randomness.

On the contrary, the increase of solution temperature can have a negative effect on the adsorption process. For example, the increase in solution temperature can increase the solubility of hydrophobic adsorbates thus limiting the hydrophobic interactions between adsorbents and adsorbates. The increase of solution temperature can also increase the vibrational energy of adsorbates on adsorbents thus promoting desorption.[27] However, these negative effects are mostly overridden by the enhanced diffusion at higher temperature which leads to an overall increase in removal efficiency.

3.6 The role of solution pH

The pH of a solution influences the adsorption performance since the physiochemical properties of adsorbents and adsorbates are strongly pH dependent. The increase in pH leads to the decrease of PFOA and PFOS adsorption capacity due to the enhanced electrostatic interaction and hydrogen bonding between positively charged MOF nodes and negatively charged PFAS combined with less competition from OH^- at

acidic condition. The respective pK_a of PFOA and PFOS are -0.5 and -3.3, rendering them negatively charged at environmentally relevant pH (e.g., pH = 3 - 10) thus they are typically referred to as anionic PFAS. Other examples of anionic PFAS are the PFCA (e.g., PFBA and TFA) and PFSA (e.g., PFBS) families. The surface charge of MOFs depends on their pH_{pzc} (pH at the point of zero charge) value and a pH above or below this value indicates MOFs exhibiting a negative or positive surface charge, respectively.[27,29,35] For example, the pH_{pzc} of Basolite A100 MOF is ~9 with a positive surface charge at pH < 9. The adsorption capacity of PFOA at pH = 3.5 is higher than that at pH = 7 due to the stronger electrostatic interaction as a result of the higher positive charge at pH = 3.5. The adsorption capacity of PFOA is the lowest at pH = 10.5 because of electrostatic repulsions between the negatively charged MOF and PFOA.[27] One exception is ZIF-L which exhibits lower adsorption capacity at pH = 3 compared to pH = 5.[30] This is due to the low acidic stability of ZIF-L at pH = 3. Despite the preferable performance of MOFs at acidic environment, the solution pH should be carefully adjusted to maintain the stability of MOFs. Furthermore, hydrogen bonding can be formed between protonated MOFs and the carboxylate and sulfonate headgroups of PFOA and PFOS at pH below pH_{pzc}, resulting in larger adsorption capacities.[29,38] Moreover, the increase in pH signifies the increase of OH^- concentration which can compete with PFOA for MOF binding sites due to the stronger binding energy between OH^- and the metal node (e.g., Fe_3O for MIL-101-Fe).[29] It is important to note that the role of pH on the adsorption capacity of non-ionic PFAS is likely to change compared to anionic PFAS since the charge state of non-ionic PFAS evolves with pH (unlike anionic PFAS constantly carrying negative charge) which will alter the adsorption mechanism (in particular, electrostatic interactions). For example, the pK_a value of FOSA is estimated to be in the range of 3.3 - 7.0, rendering it non-ionic at circumneutral pH and negatively charged at basic environments (e.g., pH = 9).[52,53] The increase of solution pH to above 7 would enhance the electrostatic interaction between cationic MOFs and negatively charged FOSA.

3.7 The role of water matrix

The presence of co-existing anions (e.g., Cl^-, NO_3^-, SO_4^{2-}, CO_3^{2-}, and $HCrO_4^-$) can lead to a compromised adsorption performance of anionic PFAS for most MOFs, in particular MOFs featuring an electrostatic interaction mechanism due to the competition for adsorption sites and/or the reduction in PFAS solubility. The electrostatic attraction between the adsorbent and adsorbate will be weakened with increasing ionic strength. Furthermore, the addition of salt mixtures may lead to the decrease of PFOA adsorption capacity due to decreasing solubility of PFOA (called salting out effect).[32] One exception is Cl^- which has a negligible effect on defective UiO-66 prepared with HCl as modulator due to the high local Cl^- concentration already existing within the MOF pores.[35] The effect of humic acid on anionic PFAS adsorption is similar to the anion case where its presence reduces the adsorption capacity. Despite the competitions from anions, MOFs can still achieve significant removal of PFAS considering the large adsorption capacity and high selectivity toward PFAS due to the synergistic effect of multiple mechanisms. For example, as high as 74% of PFOS can still be removed by SCU-8 in the presence of anions that are in large excess, which is noticeably larger than other adsorbents such as zeolite and PAC.[31] MOFs are also promising platforms for the simultaneous removal of PFAS and co-existing harmful anions such as CrO_4^{2-} and $Cr_2O_7^{2-}$ from wastewater. [35]

Cations such as Ca^{2+} and Fe^{3+} positively affect the adsorption capacity of PFOA and PFOS because those cations can act as bridge between neighboring PFOA molecules thereby enhancing their adsorption capacity.[27,28] In addition, increasing Fe^{3+} concentrations can increase not only the degree but also the size of Fe^{3+}-PFOS complexation as confirmed by thermodynamic analysis and density functional theory (DFT) calculations. Moreover, Fe^{3+} may neutralize the negative surface charge on the MOF surfaces and promotes the formation of salt-bridge formations between MOF and PFOS.[28]

Most studies used lab-prepared water consisting of either PFOA or PFOS as the target compound. However, it is widely known that the performance of adsorbents is strongly associated with the respective water chemistry. Li *et al.* treated PFAS-contaminated groundwater collected from 11 U.S. Air Force installations using NU-1000 and found that the removal of anionic PFAS varied significantly depending on

the water matrix.[25] Results from a statistical Spearman correlation analysis reveals the removal of anionic PFAS exhibits a strong negative correlation with total conductivity, alkalinity, and hardness as the existence of anions and cations compete or weaken the electrostatic adsorbent and adsorbate interactions. The role of total organic carbon (TOC) is negatively correlated with anionic PFAS removal, but its role is not significant. On the other hand, this statistical analysis further reveals the adsorption of non-ionic PFAS is negatively correlated with conductivity, total alkalinity, hardness and positively correlated with TOC but their effects are not statistically significant due to the dominant Lewis acid-base interactions.

4. Regeneration of MOFs

The reusability of an adsorbent is of great importance since it is directly related to the economic cost for practical water remediation. The regeneration process has always been extremely challenging for all types of PFAS adsorbents including the state-of-art GAC and IX resins.[55,57] For example, the high temperature requirement for the thermal regeneration of GAC may cause the decrease of their adsorption capacities and a change of GAC morphology.[58] Another example is the low regeneration percentage (< 10%) when a mixture of salts (NaCl and NaOH) was adopted for desorbing PFBS and PFOS from acrylic resins.[59] The regeneration of MOFs for PFAS treatment is underexplored and only 8 out of 17 publications have discussed the regeneration to date, but on a positive note, these few existing studies indicate that MOFs are reusable by means of chemical washings.

Common solvents for washings include salt solutions (e.g., NO_3^-, Cl^-, SO_4^{2-} and CO_3^{2-}), acidic solutions, basic solutions, organic solvents (e.g., methanol and ethanol) and binary mixtures of organic solvents containing inorganic acids, bases or salts as listed in **Table 1**. More than 90% adsorption capacity can be retained for the MIL family MOFs (e.g., MIL-101-Cr-QDMEN (**Figure 6A**), MIL-53-dimethyl 2,6-naphthalene dicarboxylate (NDC), MIL-53-Al-BPDC and Basolite A100 MOF or MIL-53-Al) with the exception of MIL-96-RHPAM2 with only 77% PFOA recovered[22,27,28,34]), NU-1000 (**Figure 6B**) [26] and F-MOF[38] after 3 to 5 adsorption-desorption cycles. FTIR, XPS, PXRD and BET analyses revealed that the respective functionalities and structural integrities are retained after regeneration compared to the pristine

MOFs. SCU-8, however, exhibited relatively low recovery with 44% adsorption capacity after 2 to 4 cycles (**Figure 6C**).[31] The choice of regeneration solvent and the corresponding desorption mechanism depends strongly on the MOF structures (e.g., node composition and organic linker type and functionality). For example, MIL-100-Cr-QDMEN and NU-1000 can be best regenerated using methanol with NaCl or HCl where the chloride anions form stronger bonds with the (unsaturated) metal nodes or protonated organic linkers compared to PFOA or PFOS.[26,34] Li *et al*. shows that SCU-8 exhibits best recovery when using a mixture of salts (NO_3^-, Cl^-, SO_2^- and CO_3^{2-}).[31] In another study, Ma *et al.* reports that F-MOF (Zn node and fluorinated H_2tfbdc linker) shows best recovery of PFOA using a methanolic alkali solution. Methanol, as a protonic solvent can form hydrogen bonding interactions with fluorine in PFOA and in addition, the alkaline methanol can readily form a salt with PFOA and thus enhancing the eluting effect.[38]

The use of organic solvents as part of the regeneration process is not ideal considering the toxicity and followed disposal of those solvents. Other less harmful solvents (e.g., mixture of salts) should be investigated for MOF regeneration with a systematic range of composition and concentration for different MOFs. In addition, the regeneration testing performed to date were all focused on anionic PFAS (PFOA, PFOS and PFBS). Similar testing is missing for non-ionic and zwitterionic PFAS where the dominant adsorption mechanisms are different. More importantly, destructive technologies (e.g., advanced oxidation/reduction processes) should be explored for the degradation of concentrated PFAS residues after adsorption by MOFs considering the toxicity of PFAS. On one hand, destructive methods should be carefully chosen to destroy PFAS molecules on loaded MOFs while maintaining the structural integrity of MOFs. On the other hand, the recovered PFAS in solvent solutions after the regeneration of MOFs can be treated by those methods for a complete solution of PFAS contamination. As a matter of fact, the state-of-art treatment approach of PFAS-contaminated water is a treatment train consisting of a passive treatment approach (e.g., adsorption) and an active treatment approach (e.g., plasma).[60] For example, Crimi *et al.* showed that the proposed treatment train can successfully remove and destruct PFOA by heat-activated persulfate oxidation of adsorbed GAC while the degradation efficiency for PFOS is low.[61] More efforts

should be taken to investigate more effective destructive methods such as plasma technology[62] for a complete solution of PFAS contamination.

5. MOFs for ultrasensitive detection of PFAS

The state-of-art analytical method trace-level PFAS detection in natural waterbodies is solid phase extraction (SPE) as a preconcentration and cleaning step followed by ultra-high performance liquid chromatography tandem mass spectroscopy (UPLC-MS/MS) analysis. However, the SPE process is time-consuming and can be greatly influenced by the water matrix. The often-used commercial WAX SPE cartridge is based on a weak anion exchange mechanism, rendering it vulnerable to complex water matrixes. The SPE cartridge exhibits low selectivity towards PFAS and the recovery for non-ionic PFAS is extremely low. Therefore, the development of alternative preconcentration materials which can achieve targeted capture of PFAS, and efficient enrichment is of great importance.

Taking advantage of the high selectivity towards PFAS, high adsorption capacities and tunable structures as discussed above, MOFs have recently been investigated as a preconcentration procedure coupled with electrochemical detection or chromatography such as nanoelectrospray ionization mass spectrometry (nESI-MS) and surface laser desorption/ionization time-of-flight mass spectrometry (SALDI-TOF-MS) for the ultrasensitive detection of PFAS. To date, there are a total eight studies reporting on this topic using a broad range of MOFs including ZIF-7, ZIF-8, ZIF-90,[63,64] MOF-5, MOF-235,[65] UiO-66, UiO-66(Zr)-2OH,[64,65] MIL-88-A, MIL-101-Cr,[64,66,67] PCN-222 (porous coordination network), PCN-223, PCN-224,[68] Cu-BTC MOFs,[65], BDC-based MOF,[64] $Tb_2(BDC)_3$,[64] F-MOF,[38] and LMOF-651.[69] The underlying enrichment mechanisms are similar to the adsorption process from aqueous solutions including electrostatic, hydrophobic, acid-base, and F-F interactions among others (extensively discussed in the earlier sections).

MOFs exhibit a range of advantages for pre-concentration and detection of PFAS including high selectivity, short enrichment time, low detection limit, high tolerance for complex water matrix, high signal intensity, excellent stability, and good reproducibility. Chen *et al*. report high selectivity toward PFAS and

even achieve targeted analysis of different PFAS species. They constructed a novel fluorescent sensor array comprised of PCN-222, PCN-223 and PCN-224 and found that different PFAS exhibited different fluorescence response patterns due to their diverse adsorption affinities to different PCNs.[68] However, this method was found not suitable for PFAS at low concentrations. Furthermore, MOFs generally require times in the order of minutes for the enrichment process to reach equilibrium due to synergistic effects of their large surface area, large and ordered pores and a strong surface chemistry. For example, the PCN-222, PCN-223 and PCN-224 exhibit a remarkable short response time (within 10 s).[68] MOFs coated on probes can detect PFAS around 40 times quicker as compared to the accredited analytical method and also requires around 10 time less sample (e.g., the sample preparation time according to EPA Method 537 is > 2 h).[64] Moreover, the detection limit of this approach is generally in the low ng/L level. For example, the detection limit of PFOS is 0.5 ng/L using Cr-MIL-101 as the adsorbent embedded on a microfluidic platform.[66] It should also be noted that the requirement of the sample volume is low considering the low detection limit. In comparison, the EPA method requires one liter of water sample. In addition, the application of MOFs as the preconcentration step render the procedure less sensitive to water matrix due to the high selectivity towards PFAS and large adsorption capacity. MOFs have been tested in lab-water spiked with humic acid and protein, tap water, river water, rainwater and seawater and signals show high intensity after the preconcentration step using MOFs in all cases.[64,65,68] When MOFs are coupled with other chromatographic methods, the signal intensity can be intensified. For example, a series of ZIFs was used as both the adsorbent and matrix for the SALDI-TOF-MS for the enrichment and analysis of PFOS. The characteristic peak of PFOS were detected with high signal intensity and low background interference when using a ZIF-8 matrix compared to traditional matrices.[63] Last but not least, the application of MOFs as the adsorbent and matrix displays excellent stability and reproducibility. The recovery of PFAS after the enrichment process is stable with very small standard deviation.[64,65] Considering the advanced performance of MOFs for the efficient enrichment of PFAS from aqueous solution, MOFs constitute promising materials in the field of environmental monitoring, especially for real time, rapid, accurate and on-site detection of PFAS samples.

6. Conclusions, perspectives, and recommendations

6.1 Conclusions

MOFs have been established as advanced platform for the removal of PFAS from aqueous solution as well as a preconcentration procedure coupled with analytical methods for ultrasensitive detection of PFAS. The adsorption mechanisms and performance of MOFs for PFAS removal relies heavily on the node and organic linker composition, porosity, functionality, and particle size. The best performing MOFs contain strong Lewis acid metal nodes with a high number of unsaturated sites and/or exchangeable terminally bonded ligands to promote Lewis acid-base and electrostatic interactions. The functionalization with amine and fluorine functional groups on the hydrophobic organic linkers enhances the affinity for PFAS *via* the improvement of electrostatic and hydrophobic interactions. Large surface area, pore size and volume and smaller particle size enable fast adsorption kinetics while the surface chemistry determines the overall adsorption capacity. Moreover, the structure of PFAS molecules greatly impact the adsorption mechanism and the adsorption efficiency. MOFs exhibit larger adsorption capacities for PFAS with longer C-F chain and with functional groups which are stronger Lewis bases. The underlying mechanisms for non-ionic PFAS removal are based on hydrophobic interactions (except for short- and ultrashort-chain PFAS), acid-base interactions, hydrogen bonding and van der Waals interactions. Electrostatic and/or ionic interactions play a dominant role for anionic PFAS removal among other mechanisms mentioned above, rendering anionic PFAS removal more sensitive to the water matrix. In addition, high temperature and low solution pH benefits the adsorption while MOFs can be regenerated using organic solvents and salt/acid mixtures.

6.2 Perspectives and recommendations

The structural tunability of MOFs renders them as ideal materials class for targeted PFAS removal. MOFs with anion-exchange capability (e.g., NU-1000 with its terminally coordinating hydroxo anions) have proven to show best adsorption capacities and kinetics for anionic PFAS removal. We recommend that future studies should focus on MOF classes with similar features. In addition, for practical applications, MOFs need to be sustainable and economically friendly. Thus, the cost of MOFs per unit of PFAS removal

should be evaluated in comparison with state-of-art adsorbents such as GAC. The cycle testing for regeneration and reusability should be significantly increased (>> 10 cycles) to access the lifetime of MOFs and alternative regeneration solvents should be explored and optimized to minimize the use of organic solvents. Furthermore, the long-term water stability of MOFs in given water matrices is largely unknown which should be probed in future studies. Lastly, moving from lab testing to field employment of MOFs, one should explore packed beds of MOFs in pass-through columns which might provide an engineering solution for PFAS removal instead of powdered forms used in current studies.

We also want to state general recommendations for routine PFAS testing requirements since most studies were performed using only single compound lab-prepared water with long-chain PFOA or PFOS in the absence of co-contaminants and environmentally non-relevant concentrations. There are over 5000 types of PFAS known to the scientific community and they vary significantly in chain length, functionality, and charge state and the emerging of novel ultrashort- and short-chain PFAS (e.g., GenX, PFBS, and triflate) as the replacement of long-chain PFAS in industry is not reflected in common PFAS removal studies to date. Therefore, a battery of single-compound testing is recommended exploring also ultrashort- and short-chain PFAS followed by investigations of lab-prepared mixtures using representative PFAS from diverse groups (ultrashort-, short- and long-chain, anionic, non-ionic). Notably, the concentrations of PFAS investigated in most studies to date are well beyond environmentally relevant concentrations. Thus, the use of realistic concentrations found in natural waterbodies (e.g., ng/L level for groundwater) is strongly advised. The testing of lab-prepared samples should be followed by investigations on the roles of co-contaminants (e.g., dissolved organic matter) on the performance of MOFs to further the understanding of their competition for adsorption sites. A wide choice of water sources should be considered, including but not limited to groundwater, tap water, river and lake water, industrial wastewater, etc. All analytical testing should strictly adhere to EPA method 533 (Determination of Per- and Polyfluoroalkyl Substances in Drinking Water by Isotope Dilution Anion Exchange Solid Phase Extraction and LC/MS/MS) or method 537.1 (Determination of Selected Per- and Polyfluorinated Alkyl Substances in Drinking Water by Solid Phase Extraction and LC/MS/MS).

Lastly, considering the excellent performance of MOFs for PFAS removal, we strongly encourage the research community to explore MOFs for the removal of other emerging contaminants (ECs, e.g., pharmaceuticals and personal care products, endocrine-disrupting compounds, hormones, etc.) for which no current high performing sorbents are available to date. The choice of MOF should reflect the structural features of ECs for optimal performance while the mechanisms of MOFs for PFAS removal summarized in this review might be also applicable for related ECs; and the presence of transition metals in MOFs (e.g., Ti) has the potential to facilitate the photocatalytic degradation of PFAS which represents an exciting next step in the exploration of MOFs for a complete PFAS treatment solution.

Author contributions

R.L. developed the scope of the review, conducted the literature search, wrote the first draft of this review, and designed the figures. A.N.N. co-designed the figures and edited the review. M.W. concepted, edited, and refined this review. All authors contributed to the discussion.

Conflicts of interest

There are no conflicts to declare.

Acknowledgements

M.W. gratefully acknowledges the U.S. National Science Foundation CAREER Program (award no. 1752771) and the Clarkson/SUNY ESF Healthy Water Solutions Center of Excellence (CoE) for support of this work.

References

(1) Enders, J. R.; O'Neill, G. M.; Whitten, J. L.; Muddiman, D. C. Understanding the Electrospray Ionization Response Factors of Per- and Poly-Fluoroalkyl Substances (PFAS). *Analytical and Bioanalytical Chemistry* **2022**, *414* (3), 1227–1234. https://doi.org/10.1007/s00216-021-03545-8.

(2) Kwiatkowski, C. F.; Andrews, D. Q.; Birnbaum, L. S.; Bruton, T. A.; DeWitt, J. C.; Knappe, D. R. U.; Maffini, M. v; Miller, M. F.; Pelch, K. E.; Reade, A.; Soehl, A.; Trier, X.; Venier, M.; Wagner, C. C.; Wang, Z.; Blum, A. Scientific Basis for Managing PFAS as a Chemical Class. *Environmental Science & Technology Letters* **2020**, *7* (8), 532–543. https://doi.org/10.1021/acs.estlett.0c00255.

(3) Sunderland, E. M.; Hu, X. C.; Dassuncao, C.; Tokranov, A. K.; Wagner, C. C.; Allen, J. G. A Review of the Pathways of Human Exposure to Poly- and Perfluoroalkyl Substances (PFASs) and Present Understanding of Health Effects. *Journal of Exposure Science & Environmental Epidemiology* **2019**, *29* (2), 131–147. https://doi.org/10.1038/s41370-018-0094-1.

(4) Zhang, D. Q.; Zhang, W. L.; Liang, Y. N. Adsorption of Perfluoroalkyl and Polyfluoroalkyl Substances (PFASs) from Aqueous Solution - A Review. *Science of The Total Environment* **2019**, *694*, 133606. https://doi.org/https://doi.org/10.1016/j.scitotenv.2019.133606.

(5) Du, Z.; Deng, S.; Chen, Y.; Wang, B.; Huang, J.; Wang, Y.; Yu, G. Removal of Perfluorinated Carboxylates from Washing Wastewater of Perfluorooctanesulfonyl Fluoride Using Activated Carbons and Resins. *Journal of Hazardous Materials* **2015**, *286*, 136–143. https://doi.org/https://doi.org/10.1016/j.jhazmat.2014.12.037.

(6) Olsen, G. W.; Mair, D. C.; Reagen, W. K.; Ellefson, M. E.; Ehresman, D. J.; Butenhoff, J. L.; Zobel, L. R. Preliminary Evidence of a Decline in Perfluorooctanesulfonate (PFOS) and Perfluorooctanoate (PFOA) Concentrations in American Red Cross Blood Donors. *Chemosphere* **2007**, *68* (1), 105–111. https://doi.org/https://doi.org/10.1016/j.chemosphere.2006.12.031.

(7) Deng, S.; Yu, Q.; Huang, J.; Yu, G. Removal of Perfluorooctane Sulfonate from Wastewater by Anion Exchange Resins: Effects of Resin Properties and Solution Chemistry. *Water Research* **2010**, *44* (18), 5188–5195. https://doi.org/https://doi.org/10.1016/j.watres.2010.06.038.

(8) Ding, M.; Flaig, R. W.; Jiang, H.-L.; Yaghi, O. M. Carbon Capture and Conversion Using Metal–Organic Frameworks and MOF-Based Materials. *Chem. Soc. Rev.* **2019**, *48* (10), 2783–2828. https://doi.org/10.1039/C8CS00829A.

(9) Bai, Y.; Dou, Y.; Xie, L.-H.; Rutledge, W.; Li, J.-R.; Zhou, H.-C. Zr-Based Metal–Organic Frameworks: Design, Synthesis, Structure, and Applications. *Chem. Soc. Rev.* **2016**, *45* (8), 2327–2367. https://doi.org/10.1039/C5CS00837A.

(10) Ramanayaka, S.; Vithanage, M.; Sarmah, A.; An, T.; Kim, K.-H.; Ok, Y. S. Performance of Metal–Organic Frameworks for the Adsorptive Removal of Potentially Toxic Elements in a Water System: A Critical Review. *RSC Adv.* **2019**, *9* (59), 34359–34376. https://doi.org/10.1039/C9RA06879A.

(11) Wang, C.; Liu, X.; Keser Demir, N.; Chen, J. P.; Li, K. Applications of Water Stable Metal–Organic Frameworks. *Chem. Soc. Rev.* **2016**, *45* (18), 5107–5134. https://doi.org/10.1039/C6CS00362A.

(12) Hönicke, I. M.; Senkovska, I.; Bon, V.; Baburin, I. A.; Bönisch, N.; Raschke, S.; Evans, J. D.; Kaskel, S. Balancing Mechanical Stability and Ultrahigh Porosity in Crystalline Framework Materials. *Angewandte Chemie International Edition* **2018**, *57* (42), 13780–13783.

(13) Zhang, S.; Wang, J.; Zhang, Y.; Ma, J.; Huang, L.; Yu, S.; Chen, L.; Song, G.; Qiu, M.; Wang, X. Applications of Water-Stable Metal-Organic Frameworks in the Removal of Water Pollutants: A

Review. *Environmental Pollution* **2021**, *291*, 118076. https://doi.org/https://doi.org/10.1016/j.envpol.2021.118076.

(14) Feng, M.; Zhang, P.; Zhou, H.-C.; Sharma, V. K. Water-Stable Metal-Organic Frameworks for Aqueous Removal of Heavy Metals and Radionuclides: A Review. *Chemosphere* **2018**, *209*, 783–800. https://doi.org/https://doi.org/10.1016/j.chemosphere.2018.06.114.

(15) Zhang, X.; Wang, B.; Alsalme, A.; Xiang, S.; Zhang, Z.; Chen, B. Design and Applications of Water-Stable Metal-Organic Frameworks: Status and Challenges. *Coordination Chemistry Reviews* **2020**, *423*, 213507. https://doi.org/https://doi.org/10.1016/j.ccr.2020.213507.

(16) Drout, R. J.; Robison, L.; Chen, Z.; Islamoglu, T.; Farha, O. K. Zirconium Metal–Organic Frameworks for Organic Pollutant Adsorption. *Trends in Chemistry* **2019**, *1* (3), 304–317. https://doi.org/https://doi.org/10.1016/j.trechm.2019.03.010.

(17) Wen, Y.; Zhang, P.; Sharma, V. K.; Ma, X.; Zhou, H.-C. Metal-Organic Frameworks for Environmental Applications. *Cell Reports Physical Science* **2021**, *2* (2), 100348. https://doi.org/https://doi.org/10.1016/j.xcrp.2021.100348.

(18) Islamoglu, T.; Chen, Z.; Wasson, M. C.; Buru, C. T.; Kirlikovali, K. O.; Afrin, U.; Mian, M. R.; Farha, O. K. Metal–Organic Frameworks against Toxic Chemicals. *Chemical Reviews* **2020**, *120* (16), 8130–8160. https://doi.org/10.1021/acs.chemrev.9b00828.

(19) Zango, Z. U.; Jumbri, K.; Sambudi, N. S.; Ramli, A.; Abu Bakar, N. H. H.; Saad, B.; Rozaini, M. N. H.; Isiyaka, H. A.; Jagaba, A. H.; Aldaghri, O.; Sulieman, A. A Critical Review on Metal-Organic Frameworks and Their Composites as Advanced Materials for Adsorption and Photocatalytic Degradation of Emerging Organic Pollutants from Wastewater. *Polymers (Basel)* **2020**, *12* (11). https://doi.org/10.3390/polym12112648.

(20) Russo, V.; Hmoudah, M.; Broccoli, F.; Iesce, M. R.; Jung, O.-S.; di Serio, M. Applications of Metal Organic Frameworks in Wastewater Treatment: A Review on Adsorption and Photodegradation. *Frontiers in Chemical Engineering* **2020**, *2*, 15. https://doi.org/10.3389/fceng.2020.581487.

(21) Yuan, N.; Gong, X.; Sun, W.; Yu, C. Advanced Applications of Zr-Based MOFs in the Removal of Water Pollutants. *Chemosphere* **2021**, *267*, 128863. https://doi.org/https://doi.org/10.1016/j.chemosphere.2020.128863.

(22) Mohd Azmi, L. H.; Williams, D. R.; Ladewig, B. P. Polymer-Assisted Modification of Metal-Organic Framework MIL-96 (Al): Influence of HPAM Concentration on Particle Size, Crystal Morphology and Removal of Harmful Environmental Pollutant PFOA. *Chemosphere* **2021**, *262*, 128072. https://doi.org/https://doi.org/10.1016/j.chemosphere.2020.128072.

(23) Ornstein, J. M.; Ozdemir, O. K. A Novel, Nanostructured, Metal-Organic Frameworks-Based Pretreatment Technology for the Remediation of PFAS in Industrial Wastewater. *TechConnect Briefs* **2019**, 213–216.

(24) Sini, K.; Bourgeois, D.; Idouhar, M.; Carboni, M.; Meyer, D. Metal-Organic Frameworks Cavity Size Effect on the Extraction of Organic Pollutants. *Materials Letters* **2019**, *250*, 92–95. https://doi.org/https://doi.org/10.1016/j.matlet.2019.04.113.

(25) Li, R.; Alomari, S.; Islamoglu, T.; K. Farha, O.; Fernando, S.; Mededovic Thagard, S.; M. Holsen, T.; Wriedt, M. Systematic Study on the Removal of Per- and Polyfluoroalkyl Substances from Contaminated Groundwater Using Metal–Organic Frameworks. *Environmental Science & Technology* **2021**, *55* (22), 15162–15171. https://doi.org/10.1021/acs.est.1c03974.

(26) Li, R.; Alomari, S.; Stanton, R.; Wasson, M. C.; Islamoglu, T.; Farha, O. K.; Holsen, T. M.; Thagard, S. M.; Trivedi, D. J.; Wriedt, M. Efficient Removal of Per- And Polyfluoroalkyl Substances from Water with Zirconium-Based Metal-Organic Frameworks. *Chemistry of Materials* **2021**, *33* (9), 3276–3285. https://doi.org/10.1021/acs.chemmater.1c00324.

(27) Jun, B. M.; Hwang, H. S.; Heo, J.; Han, J.; Jang, M.; Sohn, J.; Park, C. M.; Yoon, Y. Removal of Selected Endocrine-Disrupting Compounds Using Al-Based Metal Organic Framework: Performance and Mechanism of Competitive Adsorption. *Journal of Industrial and Engineering Chemistry* **2019**, *79*, 345–352. https://doi.org/https://doi.org/10.1016/j.jiec.2019.07.009.

(28) Zhao, C.; Xu, Y.; Xiao, F.; Ma, J.; Zou, Y.; Tang, W. Perfluorooctane Sulfonate Removal by Metal-Organic Frameworks (MOFs): Insights into the Effect and Mechanism of Metal Nodes and Organic Ligands. *Chemical Engineering Journal* **2021**, *406*, 126852. https://doi.org/https://doi.org/10.1016/j.cej.2020.126852.

(29) Yang, Y.; Zheng, Z.; Ji, W.; Xu, J.; Zhang, X. Insights to Perfluorooctanoic Acid Adsorption Micro-Mechanism over Fe-Based Metal Organic Frameworks: Combining Computational Calculation with Response Surface Methodology. *Journal of Hazardous Materials* **2020**, *395*, 122686. https://doi.org/https://doi.org/10.1016/j.jhazmat.2020.122686.

(30) Chen, M. J.; Yang, A. C.; Wang, N. H.; Chiu, H. C.; Li, Y. L.; Kang, D. Y.; Lo, S. L. Influence of Crystal Topology and Interior Surface Functionality of Metal-Organic Frameworks on PFOA Sorption Performance. *Microporous and Mesoporous Materials* **2016**, *236*, 202–210. https://doi.org/https://doi.org/10.1016/j.micromeso.2016.08.046.

(31) Li, Y.; Yang, Z.; Wang, Y.; Bai, Z.; Zheng, T.; Dai, X.; Liu, S.; Gui, D.; Liu, W.; Chen, M.; Chen, L.; Diwu, J.; Zhu, L.; Zhou, R.; Chai, Z.; Albrecht-Schmitt, T. E.; Wang, S. A Mesoporous Cationic Thorium-Organic Framework That Rapidly Traps Anionic Persistent Organic Pollutants. *Nature Communications* **2017**, *8* (1), 1354. https://doi.org/10.1038/s41467-017-01208-w.

(32) Sini, K.; Bourgeois, D.; Idouhar, M.; Carboni, M.; Meyer, D. Metal–Organic Framework Sorbents for the Removal of Perfluorinated Compounds in an Aqueous Environment. *New J. Chem.* **2018**, *42* (22), 17889–17894. https://doi.org/10.1039/C8NJ03312A.

(33) Barpaga, D.; Zheng, J.; Sung Han, K.; A. Soltis, J.; Shutthanandan, V.; Basuray, S.; Peter McGrail, B.; Chatterjee, S.; Kishan Motkuri, R. Probing the Sorption of Perfluorooctanesulfonate Using Mesoporous Metal–Organic Frameworks from Aqueous Solutions. *Inorganic Chemistry* **2019**, *58* (13), 8339–8346. https://doi.org/10.1021/acs.inorgchem.9b00380.

(34) Liu, K.; Zhang, S.; Hu, X.; Zhang, K.; Roy, A.; Yu, G. Understanding the Adsorption of PFOA on MIL-101(Cr)-Based Anionic-Exchange Metal–Organic Frameworks: Comparing DFT Calculations with Aqueous Sorption Experiments. *Environmental Science & Technology* **2015**, *49* (14), 8657–8665. https://doi.org/10.1021/acs.est.5b00802.

(35) Clark, C.; A.; N. Heck, K.; D. Powell, C.; S. Wong, M. Highly Defective UiO-66 Materials for the Adsorptive Removal of Perfluorooctanesulfonate. *ACS Sustainable Chemistry & Engineering* **2019**, *7* (7), 6619–6628. https://doi.org/10.1021/acssuschemeng.8b05572.

(36) Endoh, M.; Konno, H. Amino-Functionalized UiO-66 as a Novel Adsorbent for Removal of Perfluorooctane Sulfonate from Aqueous Solution. *Chemistry Letters* **2021**, *50* (8), 1592–1596. https://doi.org/10.1246/cl.210233.

(37) Konno, H.; Nakasaka, Y.; Yasuda, K.; Omata, M.; Masuda, T. Surfactant-Assisted Synthesis of Nanocrystalline Zeolitic Imidazolate Framework 8 and 67 for Adsorptive Removal of Perfluorooctane Sulfonate from Aqueous Solution. *Catalysis Today* **2020**, *352*, 220–226. https://doi.org/https://doi.org/10.1016/j.cattod.2019.12.036.

(38) Ma, S.-Y.; Wang, J.; Fan, L.; Duan, H.-L.; Zhang, Z.-Q. Preparation of a Fluorinated Metal-Organic Framework and Its Application for the Dispersive Solid-Phase Extraction of Perfluorooctanoic Acid. *Journal of Chromatography A* **2020**, *1611*, 460616. https://doi.org/https://doi.org/10.1016/j.chroma.2019.460616.

(39) Pauletto, P. S.; Bandosz, T. J. Activated Carbon versus Metal-Organic Frameworks: A Review of Their PFAS Adsorption Performance. *Journal of Hazardous Materials* **2022**, *425*, 127810. https://doi.org/https://doi.org/10.1016/j.jhazmat.2021.127810.

(40) Joseph, L.; Jun, B.-M.; Jang, M.; Park, C. M.; Muñoz-Senmache, J. C.; Hernández-Maldonado, A. J.; Heyden, A.; Yu, M.; Yoon, Y. Removal of Contaminants of Emerging Concern by Metal-Organic Framework Nanoadsorbents: A Review. *Chemical Engineering Journal* **2019**, *369*, 928–946. https://doi.org/https://doi.org/10.1016/j.cej.2019.03.173.

(41) Dhaka, S.; Kumar, R.; Deep, A.; Kurade, M. B.; Ji, S.-W.; Jeon, B.-H. Metal–Organic Frameworks (MOFs) for the Removal of Emerging Contaminants from Aquatic Environments. *Coordination Chemistry Reviews* **2019**, *380*, 330–352. https://doi.org/https://doi.org/10.1016/j.ccr.2018.10.003.

(42) Rojas, S.; Horcajada, P. Metal–Organic Frameworks for the Removal of Emerging Organic Contaminants in Water. *Chemical Reviews* **2020**, *120* (16), 8378–8415. https://doi.org/10.1021/acs.chemrev.9b00797.

(43) Hu, Y.; Guo, M.; Zhang, S.; Jiang, W.; Xiu, T.; Yang, S.; Kang, M.; Dongye, Z.; Li, Z.; Wang, L. Microwave Synthesis of Metal-Organic Frameworks Absorbents (DUT-5-2) for the Removal of PFOS and PFOA from Aqueous Solutions. *Microporous and Mesoporous Materials* **2022**, *333*, 111740. https://doi.org/10.1016/j.micromeso.2022.111740.

(44) Li, H.; Eddaoudi, M.; O'Keeffe, M.; Yaghi, O. M. Design and Synthesis of an Exceptionally Stable and Highly Porous Metal-Organic Framework. *Nature* **1999**, *402* (6759), 276–279. https://doi.org/10.1038/46248.

(45) Hong, D.-Y.; Hwang, Y. K.; Serre, C.; Ferey, G.; Chang, J.-S. Porous Chromium Terephthalate MIL-101 with Coordinatively Unsaturated Sites: Surface Functionalization, Encapsulation, Sorption and Catalysis. *Advanced Funtional Materials* **2009**, No. 19, 1537–1552.

(46) Cavka, J. H.; Jakobsen, S.; Olsbye, U.; Guillou, N.; Lamberti, C.; Bordiga, S.; Lillerud, K. P. A New Zirconium Inorganic Building Brick Forming Metal Organic Frameworks with Exceptional Stability. *J Am Chem Soc* **2008**, *130* (42), 13850–13851. https://doi.org/10.1021/ja8057953.

(47) Islamoglu, T.; Otake, K.; Li, P.; Buru, C. T.; Peters, A. W.; Akpinar, I.; Garibay, S. J.; Farha, O. K. Revisiting the Structural Homogeneity of NU-1000, a Zr-Based Metal–Organic Framework. *Cryst Eng Comm* **2018**, *20* (39), 5913–5918. https://doi.org/10.1039/C8CE00455B.

(48) Park, K. S.; Ni, Z.; Cô, A. P.; Choi, J. Y.; Huang, R.; Uribe-Romo, F. J.; Chae, H. K.; O'keeffe, M.; Yaghi, O. M. Exceptional Chemical and Thermal Stability of Zeolitic Imidazolate Frameworks. *Proceedings of the National Academy of Sciences* **2006**, *103* (27), 10186–10191.

(49) Yildiz, C.; Kutonova, K.; Oßwald, S.; Titze-Alonso, A.; Bitzer, J.; Bräse, S.; Kleist, W. Post-synthetic Modification of DUT-5-based Metal Organic Frameworks for the Generation of Single-site Catalysts and Their Application in Selective Epoxidation Reactions. *ChemCatChem* **2020**, *12* (4), 1134–1142.

(50) Hu, X.; Lou, X.; Li, C.; Ning, Y.; Liao, Y.; Chen, Q.; Mananga, E. S.; Shen, M.; Hu, B. Facile Synthesis of the Basolite F300-like Nanoscale Fe-BTC Framework and Its Lithium Storage Properties. *RSC Advances* **2016**, *6* (115), 114483–114490. https://doi.org/10.1039/C6RA22738D.

(51) Islamoglu, T.; Idrees, K. B.; Son, F. A.; Chen, Z.; Lee, S.-J.; Li, P.; Farha, O. K. Are You Using the Right Probe Molecules for Assessing the Textural Properties of Metal–Organic Frameworks? *Journal of Materials Chemistry A* **2022**, *10* (1), 157–173. https://doi.org/10.1039/D1TA08021K.

(52) Wang, R.; Ching, C.; R. Dichtel, W.; E. Helbling, D. Evaluating the Removal of Per- and Polyfluoroalkyl Substances from Contaminated Groundwater with Different Adsorbents Using a Suspect Screening Approach. *Environmental Science & Technology Letters* **2020**, *7* (12), 954–960. https://doi.org/10.1021/acs.estlett.0c00736.

(53) Nguyen, T. M. H.; Bräunig, J.; Thompson, K.; Thompson, J.; Kabiri, S.; Navarro, D. A.; Kookana, R. S.; Grimison, C.; Barnes, C. M.; Higgins, C. P.; McLaughlin, M. J.; Mueller, J. F. Influences of Chemical Properties, Soil Properties, and Solution PH on Soil–Water Partitioning Coefficients of Per- and Polyfluoroalkyl Substances (PFASs). *Environmental Science & Technology* **2020**, *54* (24), 15883–15892. https://doi.org/10.1021/acs.est.0c05705.

(54) Rudzinski, W.; Plazinski, W. Studies of the Kinetics of Solute Adsorption at Solid/Solution Interfaces: On the Possibility of Distinguishing between the Diffusional and the Surface Reaction Kinetic Models by Studying the Pseudo-First-Order Kinetics. *The Journal of Physical Chemistry C* **2007**, *111* (41), 15100–15110. https://doi.org/10.1021/jp073249c.

(55) Gagliano, E.; Sgroi, M.; Falciglia, P. P.; Vagliasindi, F. G. A.; Roccaro, P. Removal of Poly- and Perfluoroalkyl Substances (PFAS) from Water by Adsorption: Role of PFAS Chain Length, Effect of Organic Matter and Challenges in Adsorbent Regeneration. *Water Research* **2020**, *171*, 115381. https://doi.org/https://doi.org/10.1016/j.watres.2019.115381.

(56) Du, Z.; Deng, S.; Bei, Y.; Huang, Q.; Wang, B.; Huang, J.; Yu, G. Adsorption Behavior and Mechanism of Perfluorinated Compounds on Various Adsorbents—A Review. *Journal of Hazardous Materials* **2014**, *274*, 443–454. https://doi.org/https://doi.org/10.1016/j.jhazmat.2014.04.038.

(57) Sonmez Baghirzade, B.; Zhang, Y.; Reuther, J. F.; Saleh, N. B.; Venkatesan, A. K.; Apul, O. G. Thermal Regeneration of Spent Granular Activated Carbon Presents an Opportunity to Break the Forever PFAS Cycle. *Environmental Science & Technology* **2021**, *55* (9), 5608–5619. https://doi.org/10.1021/acs.est.0c08224.

(58) Watanabe, N.; Takata, M.; Takemine, S.; Yamamoto, K. Thermal Mineralization Behavior of PFOA, PFHxA, and PFOS during Reactivation of Granular Activated Carbon (GAC) in Nitrogen Atmosphere. *Environmental Science and Pollution Research* **2018**, *25* (8), 7200–7205. https://doi.org/10.1007/s11356-015-5353-2.

(59) Carter, K. E.; Farrell, J. Removal of Perfluorooctane and Perfluorobutane Sulfonate from Water via Carbon Adsorption and Ion Exchange. *Separation Science and Technology* **2010**, *45* (6), 762–767. https://doi.org/10.1080/01496391003608421.

(60) Lu, D.; Sha, S.; Luo, J.; Huang, Z.; Zhang Jackie, X. Treatment Train Approaches for the Remediation of Per- and Polyfluoroalkyl Substances (PFAS): A Critical Review. *Journal of Hazardous Materials* **2020**, *386*, 121963. https://doi.org/https://doi.org/10.1016/j.jhazmat.2019.121963.

(61) Crimi, M.; Holsen, T.; Bellona, C.; Divine, C.; Dickenson, E. *In Situ Treatment Train for Remediation of Perfluoroalkyl Contaminated Groundwater: In Situ Chemical Oxidation of Sorbed Contaminants (ISCO SC)*; Clarkson University Potsdam United States, 2017.

(62) Singh, R. K.; Brown, E.; Mededovic Thagard, S.; Holsen, T. M. Treatment of PFAS-Containing Landfill Leachate Using an Enhanced Contact Plasma Reactor. *Journal of Hazardous Materials* **2021**, *408*, 124452. https://doi.org/https://doi.org/10.1016/j.jhazmat.2020.124452.

(63) Yang, X.; Lin, Z.; Yan, X.; Cai, Z. Zeolitic Imidazolate Framework Nanocrystals for Enrichment and Direct Detection of Environmental Pollutants by Negative Ion Surface-Assisted Laser Desorption/Ionization Time-of-Flight Mass Spectrometry. *RSC Advances* **2016**, *6* (28), 23790–23793. https://doi.org/10.1039/C6RA00877A.

(64) Suwannakot, P.; Lisi, F.; Ahmed, E.; Liang, K.; Babarao, R.; Gooding, J. J.; Donald, W. A. Metal–Organic Framework-Enhanced Solid-Phase Microextraction Mass Spectrometry for the Direct and Rapid Detection of Perfluorooctanoic Acid in Environmental Water Samples. *Analytical Chemistry* **2020**, *92* (10), 6900–6908. https://doi.org/10.1021/acs.analchem.9b05524.

(65) Wang, S.; Niu, H.; Zeng, T.; Zhang, X.; Cao, D.; Cai, Y. Rapid Determination of Small Molecule Pollutants Using Metal-Organic Frameworks as Adsorbent and Matrix of MALDI-TOF-MS. *Microporous and Mesoporous Materials* **2017**, *239*, 390–395. https://doi.org/https://doi.org/10.1016/j.micromeso.2016.10.032.

(66) Cheng, Y. H.; Barpaga, D.; Soltis, J. A.; Shutthanandan, V.; Kargupta, R.; Han, K. S.; McGrail, B. P.; Motkuri, R. K.; Basuray, S.; Chatterjee, S. Metal–Organic Framework-Based Microfluidic Impedance Sensor Platform for Ultrasensitive Detection of Perfluorooctanesulfonate. *ACS Applied Materials & Interfaces* **2020**, *12* (9), 10503–10514. https://doi.org/10.1021/acsami.9b22445.

(67) Jia, Y.; Qian, J.; Pan, B. Dual-Functionalized MIL-101(Cr) for the Selective Enrichment and Ultrasensitive Analysis of Trace Per- and Poly-Fluoroalkyl Substances. *Analytical Chemistry* **2021**, *93* (32), 11116–11122. https://doi.org/10.1021/acs.analchem.1c01489.

(68) Chen, B.; Yang, Z.; Qu, X.; Zheng, S.; Yin, D.; Fu, H. Screening and Discrimination of Perfluoroalkyl Substances in Aqueous Solution Using a Luminescent Metal–Organic Framework Sensor Array. *ACS Applied Materials & Interfaces* **2021**, *13* (40), 47706–47716. https://doi.org/10.1021/acsami.1c15528.

(69) Yin, H.-Q.; Tan, K.; Jensen, S.; Teat, S. J.; Ullah, S.; Hei, X.; Velasco, E.; Oyekan, K.; Meyer, N.; Wang, X.-Y.; Thonhauser, T.; Yin, X.-B.; Li, J. A Switchable Sensor and Scavenger: Detection and Removal of Fluorinated Chemical Species by a Luminescent Metal-Organic Framework. *Chem Sci* **2021**, *12* (42), 14189—14197. https://doi.org/10.1039/d1sc04070g.

Abbreviations

MOF families
MOFs Metal-organic frameworks
MIL Materials of Institute Lavoisier
UiO University of Oslo
NU Northernwestern University
ZIF Zeolitic imidazolate framework
SCU Soochow University
DUT Dresden University of Technology
PCN Porous coordination network

Ligands
BTC Benzenetricarboxylic
BPDC Biphenyl-4,4'-dicarboxylic acid
NDC Dimethyl 2,6-naphthalene dicarboxylate
BDC Terephthalic acid
RHPAM Hydrolyzed polyacrylamide
QDMEN Quaternized *N*,*N*-dimethylethylenediamine

PFAS families
PFAS Per- and polyfluoroalkyl substances
PFCA Perfluorinated carboxylic acid
PFDA Perfluorodecanoic acid
PFNA Perfluorononanoic acid
PFOA Perfluorooctanoic acid
PFHpA Perfluoroheptanoic acid
PFHxA Perfluorohexanoic acid
PFPeA Perfluoropentanoic acid
PFBA Perfluorobutanoic acid
TFA Trifluoroacetic acid
PFSA Perfluorosulfonic acid
PFDS Perfluorodecane sulfonate
PFNS Perfluorononane sulfonate
PFOS Perfluorofluorooctane sulfonate
PFHpS Perfluoroheptane sulfonate
PFHxS Perfluorohexane sulfonate
PFPeS Perfluoropentane sulfonate
PFBS Perfluorobutane sulfonate
FTS Fluorotelomer sulfonic acid
FTCA Fluorotelomer carboxylic acids
FPePA 5:3 3-perfluoropentyl propanoic acid
FHEA 6:2 2-perfluorohexyl ethanoic acid
FASAA Perfluoroalkane sulfonamide acetic acid

FBSAA Perfluorobutanesulfonamide acetic acid
MeFOSAA N-Methyl perfluorooctane sulfonamide acetic acid
FASA Perfluoroalkane sulfonamide
FBSA Perfluorobutanesulfonamide
FHxSA Perfluorohexanesulfonamide
FOSA Perfluorooctanesulfonamide
MeFASA N-Methyl perfluoroalkane sulfonamide
MeFBSA N-Methyl perfluorobutanesulfonamide
MeFOSA N-Methyl perfluorooctane sulfonamide
Am-Pr-FASA N-[3-(dimethylamino)propyl]- perfluoroalkane sulfonamide
PBSaAm N-[3-(dimethylamino)propyl]-perfluorobutane-1-sulfonamide
PFHxSaAm N-[3-(dimethylamino)propyl]-perfluorohexane-1-sulfonamide
PFOH Perfluorinated alcohol

Other abbreviations
EPA Environmental Protection Agency
IX Ion-exchange
GAC Granular activated carbon
PAC Powdered activated carbon
COF Covalent-organic frameworks
BET Brunauer-Emmett-Teller
FTIR Frontier-transform infrared spectroscopy
XPS X-ray photoelectron spectroscopy
SEM Scanning electron microscopy
PXRD Powder X-ray diffraction
DRIFTS diffuse reflectance infrared Frontier-transform spectroscopy
CUS Coordinated unsaturated sites
CMC Critical micelle concentration
DFT Density functional theory
TOC Total organic carbon
SPE Solid phase extraction
UPLC-MS/MS Ultra-high performance liquid chromatography- tandem mass spectroscopy
nESI-MS nanoelectrospray ionization mass spectrometry
SALDI-TOF-MS Surface laser desorption/ionization time-of-flight mass spectrometry

Scheme 1. Schematic representation displaying most common PFAS sources with their resulting environmental contaminations and adverse health effects. Can MOFs be considered as solution for this anthropogenic problem?

Figure 1. Crystal structures of MOFs discussed in this review for PFAS adsorption. Metal node composition (*left*), packing diagram displaying the pores (*middle*) and Lewis structures of organic linkers (*right*). The color code is as follows: Zn, green; Co, pink; Zr, cyan; Th, green; Al, purple; Ti, orange; Cr/Fe, lavender; C, gray and N, blue. The large colored spheres represent the pores of respective MOFs. All crystal structures were generated using the crystallographic coordinates retrieved from the CSD.

Figure 2. Molecular structures of investigated PFAS.

Figure 3. (A-C) Adsorption kinetics and (D-F) isotherms of PFOA on (functionalized) MIL-101-Cr, PFOA and PFOS on UiO-66 and UiO-67, and PFOA on Fe-based MOFs. Reprinted with permission from Liu *et al*., 2015.[34] Copyright 2015, American Chemical Society. Sini *et al*., 2019.[24] Copyright 2019, Royal Society of Chemistry; Yang *et al*., 2020.[29] Copyright 2020, Elsevier.

Figure 4. Structural characterization of NU-1000 before (blue) and after (red) saturation with PFBS: (A) N_2 adsorption isotherms at 77 K with the respective BET surface areas, with desorption points omitted for the sake of clarity; (B) DFT pore size distribution plots with the respective pore volumes; (C) FTIR spectra; (D) SEM images; (E) PXRD patterns; (F) DRIFTS spectra. Reprinted with permission from Li *et al*., 2021.[26] Copyright 2021, American Chemical Society.

Figure 5. Structural characteristics of PFAS@MOF adsorption mechanisms: (A) DFT optimized geometries of PFBS—pyrene linker—Zr_6 node domains of PFBS@NU-1000 and zoomed-in view on respective adsorption sites with dashed lines representing hydrogen bonding and electrostatic interactions of RSO_3—Zr_6 motifs; (B) interactions between PFOA and Basolite A100 featuring electrostatic, hydrophobic interactions, hydrogen bonding and coordination by Al^{3+}; (C) electrostatic interaction between the cationic metal node of MIL-53(Al) and anionic PFOS; (D) Lewis acid/base complexes between PFOA and Fe_3O cluster (*left*) and protonated Fe_3O cluster (*right*). Reprinted with permission from Li *et al*., 2021.[26] Copyright 2021, American Chemical Society; Jun *et al*., 2019.[27] Copyright 2019, Elsevier; Zhao *et al*., 2021.[28] Copyright 2021, Elsevier; Yang *et al*., 2020.[29] Copyright 2020, Elsevier.

Scheme 2. Schematic representation of various factors effecting PFAS adsorption in MOFs

Figure 6. Removal of (A) PFOA by MIL-101(Cr)-QDMEN, (B) PFBS by NU-1000 and (C) PFOS by SCU-8 in successive adsorption cycles. Reprinted with permission from Liu *et al*., 2015.[34] Copyright 2015, American Chemical Society; Li *et al.*, 2021.[26] Copyright 2021, American Chemical Society; Li *et al*., 2017.[31] Copyright 2017, Nature.

Table 1. Structural features of MOFs investigated for PFAS adsorption and comparison of their adsorption and regeneration performance.

MOF	Metal ion in the node	Linker	BET surface area (m^2/g)	Pore volume (cm^3/g)	Structural features of MOFs	PFAS tested	MOF dosage (g/L)	PFAS concentration (mg/L)	pH	PFAS adsorption kinetics[1]	PFAS adsorption capacity[2] (mg/g)	Regeneration solvent	Regeneration performance	Ref.
MIL-101-Cr	Cr(III)	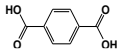	2560	1.68	Quasi-spherical cages, pore sizes 2.9 and 3.4 nm; apertures 1.2 and 1.6 nm	PFOA	0.1	1000	5	K_2 = 0.00014 g mg^{-1} min^{-1}, t_e < 60 min	460	N.A.[3]	N.A.	34
MIL-101-Cr-NH_2	Cr(III)	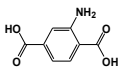	1195	2.0	Quasi-spherical cages, pore sizes 2.9 and 3.4 nm; apertures 1.2 and 1.6 nm	PFOA	0.1	1000	5	K_2 = 0.00015 g mg^{-1} min^{-1}, t_e < 60 min	290	N.A.	N.A.	
MIL-101-Cr-NMe_3	Cr(III)	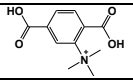	445	N.A.	N.A.	PFOA	0.1	1000	5	K_2 = 0.00016 g mg^{-1} min^{-1}, t_e < 60 min	493	N.A.	N.A.	
MIL-101-Cr-DMEN	Cr(III)	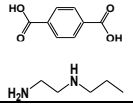	1692	N.A.	N.A.	PFOA	0.1	1000	5	K_2 = 0.00011 g mg^{-1} min^{-1}, t_e < 60 min	534	N.A.	N.A.	
MIL-101-Cr-QDMEN	Cr(III)	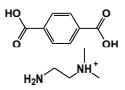	1530	N.A.	N.A.	PFOA	0.1	1000	5	K_2 = 0.00021 g mg^{-1} min^{-1}, t_e < 60 min	754	1% NaCl/methanol (30/70, v/v),	90% capacity after 3 uses	
ZIF-7	Zn(II)		14	0.207	3D porous structure, SOD topology, pore size 0.3 nm	PFOA	0.2	207	5	t_e > 60 min	22	N.A.	N.A.	30
ZIF-8	Zn(II)		1291	0.663	3D porous structure, SOD topology, pore size 1.16 nm	PFOA	0.2	207	5	t_e > 60 min	177	N.A.	N.A.	
ZIF-L	Zn(II)		12	0.066	Like SOD topology with 2D layers bridged by N-H···N hydrogen bonds of non-coordinating ligands, pore size 0.34 nm	PFOA	0.2	207	5	t_e < 60 min	244	N.A.	N.A.	
SCU-8	Th(IV)	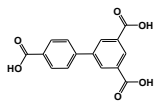	1360	0.87	3D open-framework structure with 1D hexagonal tubular channels of 2.2 × 2.2 nm size, (4,8) connected binodal flu topology	PFOS	5	1	6.3	t_e < 10 min	45	mixed salt solution containing 1.25% NO_3^-, 1.25% Cl^-, 1.25% SO_4^{2-}, and 1.25% CO_3^{2-}	44% removal for cycles 2 - 4	31
UiO-66	Zr(IV)	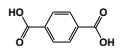	682	0.56	3D porous structure, pore sizes 0.8 and 1.1 nm, fcu topology	PFOA	1	500	4	K_2 = 0.00273 g mg^{-1} min^{-1}, $t_e \approx$ 10 min	388	N.A.	N.A.	32
						PFOS		500	4	K_2 = 0.00665 g mg^{-1} min^{-1}, $t_e \approx$ 10 min	160			

						PFO		500	N.A.	N.A.	250			
UiO-66-F4	Zr(IV)	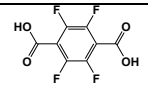	682	0.5	3D porous structure, pore sizes 0.8 and 1.1 nm, fcu topology	PFOA	1	500	4	K_2 = 0.00257 g mg^{-1} min^{-1}, $t_e \approx$ 10 min	467	N.A.	N.A.	
						PFOS		500	4	K_2 = 0.00958 mg^{-1} min^{-1}, $t_e \approx$ 10 min	254			
						PFOH		500	N.A.	N.A.	350			
Defective UiO-66-10 (prepared with 10 mL HCl as moderator)	Zr(IV)	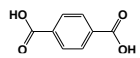	1423	0.72	3D porous structure, pore sizes of 0.8, 1.1, 1.6, and 2.0 nm, fcu topology	PFOS	0.5	500	5	K_2 = 0.00021 g mg^{-1} min^{-1}, t_e < 60 min	375	N.A.	N.A.	35
						PFBS		500		t_e<60 min	162[5]			
Defective UiO-66-25	Zr(IV)	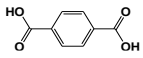	1404	0.72	3D porous structure, pore sizes of 0.8, 1.1, 1.6, and 2.0 nm, fcu topology	PFOS	0.5	500	5	K_2 = 0.00010 g mg^{-1} min^{-1}, t_e < 60 min	350	N.A.	N.A.	
						PFBS		500		t_e < 60 min	192[5]			
Cr-MIL-101	Cr(III)	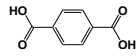	2540	1.87	3D porous structure, two distinct types of mesoporous cages (2.9 and 3.4 nm)	PFOS	10	5000	N.A.	$t_e \approx$ 125 h[6]	N.A.	N.A.	N.A.	33
Fe-MIL-101	Fe(III)	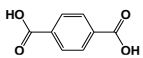	3100	2.76	3D porous structure, two distinct types of mesoporous cages (2.9 and 3.4 nm)	PFOS	10	5000	N.A.	$t_e \approx$ 250 h[6]	N.A.	N.A.	N.A.	
Basolite A100 MOF or MIL-53(Al)	Al(III)	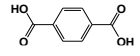	630	0.54	3D framework structure, 1D $Al(OH)_n$ chains interconnected by ligand, pore size 0.9 nm, sra topology	PFOA[4]	0.1	100	7	K_2 = 0.0073 g mg^{-1} min^{-1}, $t_e \approx$ 4 h	169	Ethanol	~ 100% capacity after 4 cycles	27
UiO-66	Zr(IV)	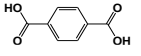	1580	0.56	3D porous structure, pore sizes 0.8 and 1.1 nm, fcu topology	PFOA	1	500	4	K_2= 0.001323 g mg^{-1} min^{-1}, t_e<60 min	388	N.A.	N.A.	24
						PFOS		500		K_2= 0.0065g mg^{-1} min^{-1}, t_e<60 min	160			
UiO-67	Zr(IV)	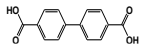	2500	0.98	3D porous structure, pore sizes 1.2 and 1.6 nm, fcu topology	PFOA	1	500	4	K_2= 0.00061 g mg^{-1} min^{-1}, t_e<60 min	743	N.A.	N.A.	
						PFOS		500		K_2= 0.00052 g mg^{-1} min^{-1}, t_e<60 min	583			
MIL-125-NH_2	Ti(IV)	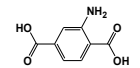	1484	0.66	3D porous structure, two types of cages (tetrahedral 0.613 nm, and octahedral 1.255 nm), aperture sizes 0.5-0.7 nm, fcu topology	PFOA	N.A.	500	N.A.	N.A.	42	N.A.	N.A.	23
						PFOS		500			17			
MIL-100-Fe	Fe(III)	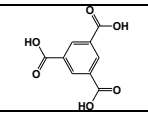	1456	1.25	3D porous structure, two types of cages (octahedral 1.255 nm, and tetrahedral 0.613 nm)	PFOA	1	1000	3.3	K_2 = 0.00001 g mg^{-1} min^{-1}, t_e > 120 min	427	N.A.	N.A.	29

MIL-101-Fe	Fe(III)	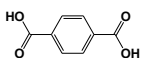	1811	1.8	3D porous structure, two types of cages (2.9 and 3.4 nm size) with 3 distinct apertures of 0.6, 1.2, 1.5 nm	PFOA	1	1000	3.3	K_2 = 0.000003 g mg^{-1} min^{-1}, t_e > 120 min	490	N.A.	N.A.	
Fe-BTC	Fe(III)	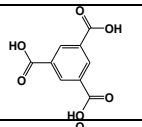	1051	1.34	Amorphous	PFOA	1	1000	3.3	K_2 = 0.000002 g mg^{-1} min^{-1}, t_e > 120 min	548	N.A.	N.A.	
Mn-BTC	Mn(II)	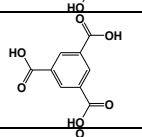	1542	N.A.	3D porous structure, details N.A.	PFOA	1	1000	3.3	N.A.	130	N.A.	N.A.	
Cu-BTC	Cu(II)	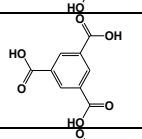	1429	0.404	3D porous structure, details N.A.	PFOA	1	1000	3.3	N.A.	95	N.A.	N.A.	
Ce-BTC	Ce(III)	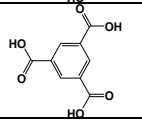	43	0.10	3D porous structure, details N.A.	PFOA	1	1000	3.3	N.A.	210	N.A.	N.A.	
MIL-53-Al	Al(III)	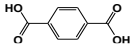	1336	0.54	3D framework structure, 1D $Al(OH)_n$ chains interconnected by ligand, pore size 0.9 nm, sra topology	PFOS	N.A.	20-80	7	K_2 = 0.00052 g mg^{-1} min^{-1}, t_e ~ 200 min	66	N.A.	N.A.	
MIL-53-Fe	Fe(III)	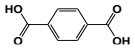	1246	0.128	3D framework structure, 1D $Fe(OH)_n$ chains interconnected by ligand, pore size 0.9 nm, sra topology	PFOS	N.A.	10-60	7	N.A.	N.A.	N.A.	N.A.	
MIL-53-Cr	Cr(III)	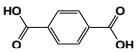	873	0.6	3D framework structure, 1D $Cr(OH)_n$ chains interconnected by ligand, pore size 0.9 nm, sra topology	PFOS	N.A.	10-60	7	N.A.	N.A.	N.A.	N.A.	
MIL-53-Al-NDC	Al(III)	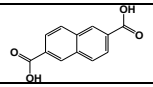	1131	N.A.	3D porous structure, details N.A.	PFOS	N.A.	20-80	7	K_2 = 0.0000012 g mg^{-1} min^{-1}, t_e = 1-2 h	171	Methanol	~100% recovery of PFOS	
MIL-53-Al-BPDC or DUT-5	Al(III)	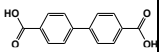	1417	N.A.	3D framework structure, 1D $Al(OH)_n$ chains interconnected by ligand, pore size 0.85 nm, sra topology	PFOS	N.A.	20-80	7	K_2 = 0.000042 g mg^{-1} min^{-1}, t_e = 1-2 h	305	Methanol	~100% recovery of PFOS	
MIL-96-RHPAM 2	Al(III)	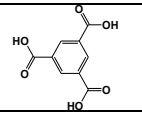	75	0.24	3D framework structure, 3 distinct cages (0.8, 0.25 -0.35, and 0.27 nm)	PFOA	1	1000	N.A.	K_2= 0.00017 g mg^{-1} min^{-1}, t_e=186 h[7]	340	Methanol/water (3:1 v/v) with 10 mM AA and 50 mM NaCl	77% PFOA recovered	22
NU-1000	Zr(IV)		2210	1.369		9 PFCAs	0.2	0.1 - 1000	N.A.	t_e ~ 1 min[8]	622 (PFOS)	30/70 v/v	96% capacity	26

						and PFSAs					547 (PFHxS) 404 (PFBS) 604 (PFDA) 507 (PFOA) 421 (PFHpA) 344 (PFPeA) 274 (PFBA) 201 (TFA)	0.1 M HCl/methanol[10]	after five cycles	
		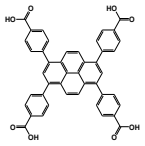			Hexagonal mesopore channels (~3.3 nm) and triangular micropore channels (~1.3 nm). Both pores are connected by 0.8 × 1 nm windows	11 PFCAs, PFSAs and FTS	0.4-1	19-258 μg/L[9]	N.A.	t_e < 30 min				
NU-1000	Zr(IV)	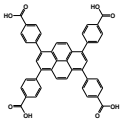	2210	1.369	Hexagonal mesopore channels (~3.3 nm) and triangular micropore channels (~1.3 nm). Both pores are connected by 0.8 × 1 nm windows	28 PFAS belonging to 8 families	0.2	0.003-260 μg/L[9]	5.3-8.0	t_e ~ 1 min[8]	N.A.	N.A.	N.A.	25
UiO-66	Zr(IV)	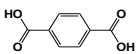	1000	0.56	3D porous structure, pore sizes 0.8 and 1.1 nm, fcu topology					t_e < 10 min				
ZIF-8	Zn(II)		2100	0.663	3D porous structure, pore size 1.16 nm, aperture 0.34 nm, SOD topology					t_e > 30 min				
UiO-66	Zr(IV)	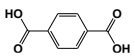	1598	0.56	3D porous structure, pore sizes 0.8 and 1.1 nm, fcu topology	PFOS	1	50-500	N.A.	N.A.	346	N.A.	N.A.	36
UiO-66-NH_2	Zr(IV)	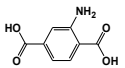	1114	0.379	3D porous structure, average pore size 1.8 nm, fcu topology	PFOS	1	50-500	N.A.	t_e ≈ 5 min	512	N.A.	N.A.	
MOF-801	Zr(IV)	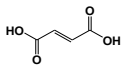	598	0.44	3D porous structure having two tetrahedral cages (0.56 nm and 0.48 nm) and one octahedral cage (0.74 nm).	PFOS	1	50-500	N.A.	N.A.	48	N.A.	N.A.	
Macro ZIF-8	Zn(II)		1530	~0.5[12]	Particle size 1.19 μm	PFOS	0.5	500	~7.0	t_e ≈ 25 h	353	N.A.	N.A.	37
Nano ZIF-8	Zn(II)		1550	~0.5[12]	Particle size 81 nm	PFOS	0.5	500	~7.0	t_e ≈ 4 h	401	N.A.	N.A.	
Macro ZIF-67	Co(II)		1610	~0.5[12]	Particle size 2.95 μm	PFOS	0.5	500	~7.0	t_e ≈ 5 h	727	N.A.	N.A.	
Nano ZIF-67	Zn(II)		1660	~0.5[12]	Particle size 150 nm	PFOS	0.5	500	~7.0	t_e < 1 h	735	N.A.	N.A.	

F-MOF	Zn(II)	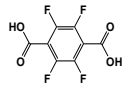	44	N.A.	3D porous structure, details N.A.	PFOA[1]	0.025	0.05-25 μg/L	2	$t_e \approx 15$ min	420	0.1% methanol alkali solution (0.1 mol L^{-1} of $NH_3 \cdot H_2O$)	91.5% to 90.8% PFOA recovered after five cycles	38
DUT-5-2	Al(III)	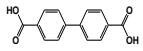	1840	0.93	3D framework structure, 1D $Al(OH)_n$ chains interconnected by ligand, pore size 0.85 nm, sra topology	PFOA	0.1	30	3-10	K_2= 0.00005 g mg^{-1} min^{-1}, $t_e \sim 600$ min	92	Methanol	93% capacity after four cycles	43
						PFOS		30	3-10	K_2= 0.000053 g mg^{-1} min^{-1}, $t_e \sim 600$ min	148	Methanol	93% capacity after four cycles	

[1]The adsorption kinetics fit the pseudo-second-order kinetic model unless otherwise specified. K_2 is the pseudo-second-order rate constant and t_e is the time needed to reach equilibrium.

[2]The adsorption isotherms fit the Langmuir model unless otherwise specified.

[3]N.A.: not available.

[4]100 mg/L BPA and 100 mg/L EE1 as co-contaminants.

[5]Freundlich isotherms.

[6]Calculated using a double exponential decay function.

[7]Calculated using a Elovich kinetics model.

[8]Adsortion kinetics were unknown due to ultrafast kinetics of NU-1000.

[9]Actual contaminated groundwater. All other tested water are lab-prepared water unless otherwise specified.

[10]The regeneration test was done using PFBS as the model compound.

[11]The ionic strength was 50% adjusted using NaCl.

[12]Erronous pore volume reported in original publication. Value corrected using Gulvirch rule.[51]

Table 2. Composition and selected physical properties of investigated PFAS.

PFAS category	C-F chain length	Acronym	Name	Formula	Molecular weight (g/mol)	pK_a[1]	Log K_{ow}
Perfluorinated carboxylic acids (PFCAs)	9	PFDA	Perfluorodecanoic acid	$CF_3(CF_2)_8COO^-$	514	-5.2	6.5
	8	PFNA	Perfluorononanoic acid	$CF_3(CF_2)_7COO^-$	464	-6.5	5.8
	7	PFOA	Perfluorooctanoic acid	$CF_3(CF_2)_6COO^-$	414	-0.50	5.1
	6	PFHpA	Perfluoroheptanoic acid	$CF_3(CF_2)_5COO^-$	364	-2.3	4.4
	5	PFHxA	Perfluorohexanoic acid	$CF_3(CF_2)_4COO^-$	314	-0.78	3.7
	4	PFPeA	Perfluoropentanoic acid	$CF_3(CF_2)_3COO^-$	264	0.34	3.0
	3	PFBA	Perfluorobutanoic acid	$CF_3(CF_2)_2COO^-$	214	1.1	2.3
	1	TFA	Trifluoroacetic acid	CF_3COO^-	114	0.23	0.79
Perfluorosulfonic acids (PFSAs)	10	PFDS	Perfluorodecane sulfonate	$CF_3(CF_2)_9SO_3^-$	600	-3.2	6.8
	9	PFNS	Perfluorononane sulfonate	$CF_3(CF_2)_8SO_3^-$	550	-3.2	6.1
	8	PFOS	Perfluorofluorooctane sulfonate	$CF_3(CF_2)_7SO_3^-$	500	-3.3	5.4
	7	PFHpS	Perfluoroheptane sulfonate	$CF_3(CF_2)_6SO_3^-$	450	-3.3	4.7
	6	PFHxS	Perfluorohexane sulfonate	$CF_3(CF_2)_5SO_3^-$	400	-3.3	4.0
	5	PFPeS	Perfluoropentane sulfonate	$CF_3(CF_2)_4SO_3^-$	350	-3.3	3.3
	4	PFBS	Perfluorobutane sulfonate	$CF_3(CF_2)_3SO_3^-$	300	-3.3	2.6
Fluorotelomer sulfonic acids (FTSs)	8	8:2 FTS	8:2 Fluorotelomer sulfonate	$CF_3(CF_2)_7(CH_2)_2SO_3^-$	527	N.A.[2]	5.7
	6	6:2 FTS	6:2 Fluorotelomer sulfonate	$CF_3(CF_2)_5(CH_2)_2SO_3^-$	427	0.36	4.4
	4	4:2 FTS	4:2 Fluorotelomer sulfonate	$CF_3(CF_2)_3(CH_2)_2SO_3^-$	327	N.A.	N.A.
	5	FPePA	5:3 3-perfluoropentyl propanoic acid	$CF_3(CF_2)_4(CH_2)_2COO^-$	341	N.A.	N.A.

Fluorotelomer carboxylic acids (FTCAs)	6	FHEA	6:2 2-perfluorohexyl ethanoic acid	$CF_3(CF_2)_5CH_2COO^-$	377	N.A.	N.A.
Perfluoroalkane sulfonamide acetic acids (FASAAs)	4	FBSAA	Perfluorobutanesulfonamide acetic acid	$CF_3(CF_2)_3SO_2NHCH_2COO^-$	356	N.A.	N.A.
	8	MeFOSAA	N-Methyl perfluorooctane sulfonamide acetic acid	$CF_3(CF_2)_7SO_2N(CH_3)CH_2COO^-$	570	N.A.	N.A.
Perfluoroalkane sulfonamides (FASAs)	4	FBSA	Perfluorobutanesulfonamide	$CF_3(CF_2)_3SO_2NH_2$	299	3.3	N.A.
	6	FHxSA	Perfluorohexanesulfonamide	$CF_3(CF_2)_5SO_2NH_2$	399	N.A.	N.A.
	8	FOSA	Perfluorooctanesulfonamide	$CF_3(CF_2)_7SO_2NH_2$	499	3.4	5.8
N-Methyl perfluoroalkane sulfonamides (MeFASAs)	4	MeFBSA	N-Methyl perfluorobutanesulfonamide	$CF_3(CF_2)_3SO_2NHCH_3$	313	N.A.	N.A.
	8	MeFOSA	N-Methyl perfluorooctane sulfonamide	$CF_3(CF_2)_7SO_2NHCH_3$	513	N.A.	6.1
N-[3-(dimethylamino)propyl]-perfluoroalkane sulfonamides (Am-Pr-FASAs)	4	PBSaAm	N-[3-(dimethylamino)propyl]-perfluorobutane-1-sulfonamide	$CF_3(CF_2)_3SO_2NH(CH_2)_3N(CH_3)_2$	384	N.A.	N.A.
	6	PFHxSaAm	N-[3-(dimethylamino)propyl]-perfluorohexane-1-sulfonamide	$CF_3(CF_2)_5SO_2NH(CH_2)_3N(CH_3)_2$	484	3.3	N.A.
Perfluorinated alcohols (PFOHs)	8	N.A.	Perfuorooctanol	$CF_3(CF_2)_7OH$	436	N.A.	N.A.

[1]The pK_a and log K_{ow} values are obtained from references 52 and 53.

[2]N.A.: not available.